Published in final edited form as:

Nature. 2019 May ; 569(7755): 284–288. doi:10.1038/s41586-019-1141-3.

Structural basis for ligand recognition at the human MT_1 melatonin receptor

Benjamin Stauch[1,†], **Linda C. Johansson**[1,†], **John D. McCorvy**[2,13], **Nilkanth Patel**[1], **Gye Won Han**[1], **Xi-Ping Huang**[2,3], **Cornelius Gati**[4,5], **Alexander Batyuk**[6], **Samuel T. Slocum**[2], **Andrii Ishchenko**[1], **Wolfgang Brehm**[7], **Thomas A. White**[7], **Nairie Michaelian**[1], **Caleb Madsen**[8], **Lan Zhu**[9], **Thomas D. Grant**[10], **Jessica M. Grandner**[1], **Anna Shiriaeva**[1], **Reid H.J. Olsen**[2], **Alexandra R. Tribo**[2], **Saïd Yous**[11], **Raymond C. Stevens**[1], **Uwe Weierstall**[8,9], **Vsevolod Katritch**[1], **Bryan L. Roth**[2,3,12,*], **Wei Liu**[9,*], **Vadim Cherezov**[1,*]

[1]Bridge Institute, Departments of Chemistry and Biological Sciences, University of Southern California, Los Angeles, CA, USA

[2]Department of Pharmacology, University of North Carolina at Chapel Hill, Chapel Hill, NC, USA

[3]National Institute of Mental Health Psychoactive Drug Screening Program (NIMH PDSP), University of North Carolina at Chapel Hill, Chapel Hill, NC, USA

[4]SLAC National Accelerator Laboratory, Bioscience Division, Menlo Park, CA, USA

[5]Stanford University, Department of Structural Biology, Stanford, CA, USA

[6]Linac Coherent Light Source, SLAC National Accelerator Laboratory, Menlo Park, CA, USA

[7]Center for Free-Electron Laser Science, DESY, Hamburg, Germany

[8]Department of Physics, Arizona State University, Tempe, AZ, USA

[9]School of Molecular Sciences and Biodesign Center for Applied Structural Discovery, Biodesign Institute, Arizona State University, Tempe, AZ, USA

[*]Correspondence should be addressed to V.C. (cherezov@usc.edu), B.L.R. (bryan_roth@med,unc.edu), and W.L. (w.liu@asu.edu).

Author contributions

B.S., L.C.J., V.K., and V.C. conceived the project, analysed data, and wrote the manuscript with contributions from all authors. B.S. and L.C.J. cloned and characterised the receptor, generated all constructs, crystallised the receptor, prepared all crystal samples and figures, solved and refined the structures, and assisted in generating mutant constructs for binding and functional analyses. B.S. designed thermostabilising point mutations and performed sequence analysis. J.D.M., X.P.H., and S.T.S. performed radioligand binding and functional experiments, assisted in generating mutant and wild-type constructs used for binding and functional analyses, analysed all binding and functional data. A.I., N.M., A.S., L.Z., and W.L. assisted in XFEL sample preparation. G.W.H. performed structure refinement and quality control. B.S., L.C.J., A.B., L.Z., W.L., and V.C. collected XFEL data. C.G., W.B., T.A.W., and T.D.G. processed XFEL data and solved the indexing ambiguity. C.M. and U.W. operated the LCP injector during XFEL data collection. N.P. performed molecular docking and molecular dynamics calculations and assisted in preparing figures. J.M.G. assisted in docking calculations. V.K. supervised molecular docking and molecular dynamics calculations. R.H.J.O. assisted with molecular biology and generating mutant constructs. A.R.T. assisted with generating mutant constructs and functional experiments. S.Y. synthesised bitopic compound, analysed data, and edited the paper. R.C.S. supervised protein expression and edited the paper. B.L.R. supervised pharmacological experiments and edited the paper. W.L. supervised the LCP crystallization and optimization experiments. V.C. coordinated and supervised the whole project.

[†]These authors contributed equally to this work

The authors declare no competing interests.

[10]Hauptman-Woodward Institute, Department of Structural Biology, Jacobs School of Medicine and Biomedical Sciences at the University at Buffalo, Buffalo, NY, USA

[11]Univ Lille, Inserm, CHU Lille, UMR-S 1172 - JPArc - Centre de Recherche Jean-Pierre AUBERT Neurosciences et Cancer, Lille, France

[12]Division of Chemical Biology and Medicinal Chemistry, Eshelman School of Pharmacy, University of North Carolina at Chapel Hill, Chapel Hill, NC, USA

[13]Current address: Department of Cell Biology, Neurobiology and Anatomy, Medical College of Wisconsin, Milwaukee, WI, USA

Abstract

Melatonin (*N*-acetyl-5-methoxytryptamine) is a neurohormone that maintains circadian rhythm[1] by synchronization to environmental cues and is involved in diverse physiological processes[2] including blood pressure and core body temperature regulation, oncogenesis, and immune function[3]. Formed in the pineal gland in a light-regulated manner[4] by enzymatic conversion from 5-hydroxytryptamine (5-HT, or serotonin), melatonin modulates sleep and wakefulness[5] by activating two high-affinity G protein-coupled receptors (GPCRs), type 1A (MT_1) and type 1B (MT_2)[3,6]. Shift work, travel, and ubiquitous artificial lighting can disrupt a natural circadian rhythm, leading to sleep disorders affecting a significant population in our modern society, posing a considerable economic burden[7]. Widely used to alleviate jet lag and as safer alternative to benzodiazepines and other sleeping aids[8,9], over-the-counter melatonin is one of the most popular supplements in the United States[10]. Here, we present high-resolution room-temperature X-ray free electron laser (XFEL) structures of MT_1 in complex with four agonists: the insomnia drug ramelteon[11], two melatonin analogues, and the mixed melatonin-serotonin antidepressant agomelatine[12,13]. The structure of MT_2 is described in an accompanying paper[14]. Despite similar endogenous ligands and dual action of agomelatine, MT_1 and 5-HT receptors differ dramatically in structure and composition of their ligand pockets, access to which in MT_1 is tightly sealed from solvent by extracellular loop 2, leaving only a narrow channel between transmembrane helices IV and V that connects it to the lipid bilayer. The binding site is extremely compact, and ligands interact with MT_1 mainly by strong aromatic stacking with F179 and auxiliary hydrogen bonds with N162 and Q181. Our structures provide an unexpected example of atypical ligand entry for a non-lipid receptor, lay the molecular foundation of ligand recognition by melatonin receptors, and will facilitate the design of future tool compounds and therapeutics, while their comparison to 5-HT receptors yields new insights into GPCR evolution and polypharmacology.

To investigate the basis of ligand recognition at MT_1, we crystallised the receptor using an intracellular loop 3 fusion with *Pyrococcus abyssi* glycogen synthase (PGS)[15]. To increase receptor thermostability, we introduced nine point mutations ($D73^{2.50}N$, $L95^{ECL1}F$, $G104^{3.29}A$, $F116^{3.41}W$, $N124^{3.49}D$, $C127^{3.52}L$, $W251^{6.48}F$, $A292^{7.50}P$, $N299^{8.47}D$, Ballesteros-Weinstein nomenclature[16] as superscripts; see Methods), which were essential for crystallisation. In combination, these modifications result in a ~40-fold reduction of melatonin affinity (~14-fold in presence of physiological concentration of sodium; Extended Data Table 1), primarily caused by the allosteric sodium site[17] mutation $D73^{2.50}N$, which is

known to affect coupling to G proteins[18], and N299$^{8.47}$D that is located in the G protein interface (Extended Data Tables 1 and 2).

MT_1 was crystallised in lipidic cubic phase (LCP) (Extended Data Fig. 1), and serial femtosecond crystallography (SFX) was used to obtain structures of MT_1 bound to the insomnia drug ramelteon (2.8 Å resolution), the high-affinity agonist 2-phenylmelatonin (2-pmt) (2.9 Å), 2-iodomelatonin, and agomelatine (both 3.2 Å). Data collection and refinement statistics for all MT_1 structures are provided in Extended Data Table 3. The overall receptor conformation in all four structures is nearly identical (Cα r.m.s.d. < 0.3 Å); therefore, we focus our analysis below on the highest resolution MT_1-ramelteon structure unless otherwise noted.

The structure of MT_1 displays the canonical GPCR topology of a heptahelical transmembrane bundle (7TM) with an extracellular N-terminus, three extracellular loops (ECL), three intracellular loops (ICL), and a short amphipathic helix VIII oriented parallel to the membrane (Fig. 1). Based on structural alignment with the active[19] and inactive states[20] of the β_2-adrenoreceptor (β_2AR), the 7TM of MT_1 is captured in an inactive conformation. Similar inactive states were observed for agonist-bound complexes without intracellular binding partners for some GPCRs that have naturally weak coupling between EC and IC sides (e.g. β_2AR), or those where this coupling was disrupted by mutations[21,22].

ECL2 forms a short β-hairpin anchored to helix III by the conserved disulfide bridge between C100$^{3.25}$ and C177^{ECL2} and a number of polar interactions with helices III, VI, and VII, tightly sealing off the extracellular entrance to the orthosteric binding site (Fig. 1), which is among the smallest of any receptor solved to date (710 Å^3, Extended Data Table 4).

Potential ligand access to the orthosteric binding site is provided by a channel between helices IV and V, opened toward the lipid bilayer (Fig. 1b, d). The channel is located about 7–11 Å below the hydrophobic membrane boundary, ~10 Å long from entrance to center of the ligand binding site, has a minimum diameter of 3 Å (about 4–5 Å otherwise), and is lined by a number of hydrophobic residues and H195$^{5.46}$, which is highly conserved in melatonin receptors.

A part of helix II that participates in shaping the ligand binding pocket contains a distinct YPYP motif (residues Y79$^{2.56}$ to P82$^{2.59}$), which introduces a bulge and kink to helix II, placing the ring planes of its tyrosine residues in antiparallel orientation (Fig. 1c). Y79$^{2.56}$ interacts with H99$^{3.24}$, while Y81$^{2.58}$ points towards the receptor core and interacts with the backbone of Y285$^{7.43}$ and the side chain of S288$^{7.46}$. This YPYP motif is unique to melatonin receptors and the closely related orphan GPR50. It is not found in any other membrane protein structures or predicted TM segments of the human proteome (see Methods). While P82$^{2.59}$ is conserved across class A (74% of receptors), an equivalent of P80$^{2.57}$ is not present in any other human GPCR[22]. Mutating any residue in the YPYP motif lowers thermostability by 6–10 °C and impairs receptor function (Extended Data Tables 5, 6), suggesting that this motif forms an important structural element of melatonin receptors that plays a role in receptor stability and activation.

Melatonergic ligands display a remarkably limited number of chemotypes. Indeed, over 80% of high-affinity melatonin ligands (from 391 compounds in ChEMBL24[23] with MT_1 affinity < 100 nM), most of which are agonists, possess a core that is either a (hetero)indene (mostly indole, benzofuran, benzoxazole) or a naphthalene bioisostere. We crystallised MT_1 with ligands from both of these major chemotypes, which together reveal the conserved receptor interaction points and pharmacophore of melatonergic ligands.

Ramelteon engages in three anchoring interactions, including aromatic stacking of its heterocyclic core with $F179^{ECL2}$ and hydrogen bonds between its alkylamide tail and $Q181^{ECL2}$ and between its dihydrofuran moiety and $N162^{4.60}$ (Fig. 2a). The methoxy and alkylamide groups of 2-pmt, 2-iodomelatonin, and agomelatine (Fig. 2b) interact with $N162^{4.60}$ and $Q181^{ECL2}$ in a similar manner as ramelteon. The ligand core forms a close contact with $G108^{3.33}$, suggesting that a larger residue in this position would clash with the ligand. Indeed, mutation $G108^{3.33}A$ practically abolishes ligand binding (Extended Data Table 5). The binding site contains a hydrophobic sub-pocket, which accommodates the phenyl and iodine substituents of the co-crystallised melatonin analogues (Fig. 2c).

Mutations of the ligand coordinating residues, $F179^{ECL2}A$ and $Q181^{ECL2}A$, are detrimental to receptor stability and activation (Extended Data Tables 5, 6), while $Q181^{ECL2}E$ is functionally better tolerated. The $N162^{4.60}A$ mutation inactivates the receptor (Extended Data Table 6) but does not affect ligand affinity and receptor stability (Extended Data Tables 1, 5), reflecting the importance of the methoxy or equivalent substituent for ligand efficacy[24]. These findings are consistent with molecular dynamics (MD) simulations of the receptor-ligand complexes (Extended Data Fig. 2), wherein equilibrium interactions between ligands and two anchor residues, $F179^{ECL2}$ and $Q181^{ECL2}$, are very stable and stronger than the interaction with $N162^{4.60}$. Taken together, these findings explain the tight steric fit and lipophilic interactions between ligands and receptor, mainly mediated by ECL2, as primary affinity determinants. The importance of ECL2 for ligand binding in melatonin receptors is further highlighted by a recent study demonstrating that transplanting the MT_1-ECL2 to GPR50, a paralogue melatonin-related receptor that does not bind melatonin[25], is sufficient to restore ligand-dependent activation in the resulting chimera[26]. Analysis of the otherwise remarkably conserved binding site shows the main difference between MT_1/MT_2 and GPR50 to occur in ECL2 (Figure 2d).

Interestingly, although residue $N255^{6.52}$ does not interact with ligands in our structures (Fig. 2a, c), and mutation $N255^{6.52}A$ does not affect ligand affinity (Extended Data Table 1), this mutation reduces receptor stability and signaling (Extended Data Tables 5, 6), suggesting potential involvement of this residue in receptor activation. Small ligands such as melatonin or agomelatine are affected more strongly by these effects than bulkier ligands (Extended Data Fig. 2e and Table 6). Intriguingly, in all our MT_1 structures we observe a small blob of electron density (~6 σ in mF_o-DF_c maps) close to $N255^{6.52}$ (Extended Data Fig. 1e). We tentatively attribute this density to propan-2-ol, an essential additive in the crystallisation of MT_1. This additive was not needed to crystallise MT_2, in which mutating $N^{6.52}$ does not affect signaling[14]. Under physiological conditions, $N255^{6.52}$ likely remains hydrated rather than directly interacting with the ligand, as also suggested by our MD simulations (Extended Data Fig. 2d).

The existence of the lateral channel is supported by studies of the bitopic ligand CTL 01–05-B-A05, a symmetrical agomelatine dimer linked by an ethoxyethane spacer (see Methods). This ligand was docked into the MT_1 binding site, indicating that it can only be accommodated if its aliphatic linker region protrudes through the channel, and, therefore, one of its monomers must pass through the channel upon binding (Fig. 3). We chose a residue in the vicinity of the channel entrance and designed a point mutation (A190$^{5.41}$F) that was predicted to keep the channel open but would interfere with placement of peripheral moieties of the bitopic ligand. Indeed, we observed that signaling for monotopic ligands is only slightly affected, whereas the bitopic ligand loses about one order of magnitude in potency (Extended Data Table 7). On the other hand, mutation A158$^{4.56}$M, designed to block the channel, causes loss of functional activity for all tested agonists, consistent with the hypothesis that the ligand entry in MT_1 is largely defined by the lateral channel.

Melatonin and serotonin are ancient molecules with physiological roles predating the evolution of nervous systems, multicellularity[27,28], and their respective appropriation as hormone and neurotransmitter. Their primordial functions resulting from their chemical properties are still evident by their occurrence in plants and their antioxidant abilities[27,28]. Structural similarity and overlapping biosynthetic pathways of melatonin and serotonin are juxtaposed by their very different pharmacological roles and physicochemical parameters. Melatonin is soluble in both water and lipid and can traverse membranes by passive diffusion, while serotonin, due to its charge, has to be secreted and actively transported[29]. Strikingly, 98% of high-affinity melatonin receptor ligands (< 100 nM in ChEMBL) are neutral at physiological pH, whereas, depending on subtype, 80–99% of 5-HT receptor ligands are charged (see Methods).

Melatonin and 5-HT receptors share a low level of sequence identity (~20–25%) and even lower binding site identity (1 out of 16 residues, Fig. 4d). A key question is how these receptor families evolved to bind structurally similar endogenous molecules while maintaining orthogonal function. Importantly, very few ligands bind both melatonin and 5-HT receptors, most notably the psychedelic alkaloid 5-methoxy-*N*/*N*-dimethyltryptamine (5-MeO-DMT)[30] and the antidepressant agomelatine[12,13], albeit with reduced potency.

The docking model of agomelatine in the 5-HT_{2C} receptor shows a similar pose to the ergotamine core[31], but has a perpendicular orientation to agomelatine in the MT_1 structure and involves completely different residues (Fig. 4). This orthogonal binding mode and the low sequence conservation between melatonin and 5-HT receptors are testament to disparate evolution driven by their distinct cognate ligands. Their receptors are co-expressed in a number of tissues[32], where promiscuous binding of endogenous molecules has to remain the exception. The two structurally similar ligands are reliably discriminated by i) structurally different binding pockets; in particular, lack in melatonin receptors of an equivalent residue to negatively charged D$^{3.32}$ that serves as primary anchor for all aminergic receptors, and ii) utilising different physical ligand properties, i.e. restricting access of charged ligands to the MT_1 binding site through the membrane channel.

In conclusion, we found the binding site of melatonin to be completely different from that of related metabolite serotonin in 5-HT receptors and an unexpected channel that provides

ligands lateral access to the receptor binding site from within the lipid bilayer. This channel represents a novel allosteric site that can be targeted by rational structure-based drug design. The atypical entry mechanism could impose constraints on ligand dimensions and physicochemical properties and can be exploited in the future development of synthetic melatonergics to address the need for safer sleeping aids without abuse potential and antidepressants that benefit from melatonin-5-HT-polypharmacology by design.

Methods

Design of thermostabilising point mutations.

The wild-type human MT_1 showed extremely low expression, yield, and stability for pursuing structural studies. To predict stabilising point mutations, the MT_1 reference sequence (UniProt[33] identifier P48039) was searched against the database of non-redundant protein sequences (nr) using the *blastp* algorithm[34,35], excluding "LOW QUALITY" and exactly identical sequences. Standard parameters were used, and alignments were scored using the BLOSUM62 matrix. The 100 closest identified homologs were aligned using COBALT[36], yielding the sequence conservation profile P_{MT1} for receptor species orthologs. Next, a conservation profile Q_{ClassA} for all transmembrane residues of human class A GPCRs (i.e., paralogous sequences) was generated using the structure-guided sequence alignment of GPCRdb[22,37]. Corresponding residues in P_{MT1} and Q_{ClassA} were mapped using the generic residue numbering of GPCRdb[37] for the sequence of human MT_1, which is contained in both alignments. For each of these residues, the dissimilarity of the two conservation profiles was quantified using the Kullback-Leibler divergence[38] $D_{KL}(P||Q)$ with $P(i)$ and $Q(i)$ being the relative frequencies of each amino acid in profiles P_{MT1} and Q_{ClassA}, respectively, for that particular residue. Residues were ranked from most to least diverging, and the top twenty most divergent residues were mutated and tested. Of all mutations identified, $A^{7.50}P$, $N^{3.49}D$, and $C^{3.52}L$ had the most beneficial effect on aSEC (analytical size-exclusion chromatography) and thermostability, and facilitated crystallisation.

Further mutations improving expression, yield, monodispersity, thermostability, or crystallisability, were $D^{2.50}N$[18,39], $G^{3.29}A$ (the most beneficial mutation out of an exhaustive Gly-to-Ala scan[40]), $F^{3.41}W$[41], $W^{6.48}F$ of the proposed rotamer toggle switch[42], $N^{8.47}D$, and $L95^{ECL1}F$ which restores a WxFG motif commonly found in class A GPCRs[43].

Crystallisation of MT_1.

The codon optimised nucleotide sequence of human MT_1 was synthesised by GenScript and subcloned into a modified pFastBac baculovirus expression vector (Invitrogen) containing an N-terminal haemagglutinin (HA) signal sequence, Flag tag, 10×His tag, and PreScission protease (PSP) cleavage site. Site directed mutagenesis was carried out using oligonucleotides (IDT) with internal mismatches and AccuPrime Pfx polymerase (Thermo Fisher Scientific) and verified by Sanger sequencing (Genewiz). After truncating 11 N-terminal (including both glycosylation sites of the receptor) and 25 C-terminal amino acids, intracellular receptor amino acid residues 219–227 were substituted by the 196-amino-acid catalytic domain of *Pyrococcus abyssi* glycogen synthase (PGS, UniProt Q9V2J8)[15]. A

number of beneficial point mutations was identified (see above), nine of which were used in the final crystallised construct (MT_1-CC).

The resulting MT_1-CC chimera was expressed in *Spodoptera frugiperda* (Sf9, purchased from ATCC, CRL-1711, authenticated by supplier using morphology and growth characteristics, certified mycoplasma-free) insect cells using the Bac-to-bac baculovirus expression system (Invitrogen). Cells with a density of (2–3) × 10^6 cells ml^{-1} were infected with baculovirus at 27 °C at a multiplicity of infection of 5, harvested by centrifugation 48 hours post infection and stored at −80 °C until use. The membrane fraction was isolated from 3 liters of biomass using repeated Dounce homogenisation and ultracentrifugation in hypotonic (twice, 10 mM HEPES pH 7.5, 10 mM $MgCl_2$, 20 mM KCl) and hypertonic (three times, 10 mM HEPES pH 7.5, 10 mM $MgCl_2$, 20 mM KCl, 1 M NaCl) buffer. After membrane isolation, ligand (ramelteon, Apex Biosciences; agomelatine, Sigma-Aldrich; 2-phenylmelatonin, Tocris; or 2-iodomelatonin, Tocris) concentration was 100 μM in all buffers.

Washed membranes were incubated in hypotonic buffer in presence of 2 mg ml^{-1} iodoacetamide (Sigma-Aldrich) for 45 minutes, and receptor was subsequently extracted from membranes in a volume of 200 ml by addition of 2× solubilisation buffer (100 mM HEPES pH 7.5, 300 mM NaCl, 2% (wt/vol) n-dodecyl-β-D-maltopyranoside (DDM, Anatrace) and 0.4% (wt/vol) cholesterol hemisuccinate (CHS, Sigma-Aldrich)) for 3 hrs. After overnight incubation with 1 ml of Talon (immobilised metal affinity chromatography, IMAC) resin (Clontech) in presence of 150 mM NaCl and 20 mM imidazole, the sample was washed on a gravity column (Bio-Rad) with 12 column volumes (cv) of wash buffer 1 (50 mM HEPES pH 7.5, 800 mM NaCl, 25 mM imidazole pH 7.5, 10 mM $MgCl_2$, 10% (vol/vol) glycerol, 0.05%/0.01% (wt/vol) DDM/CHS) followed by 6 cv of wash buffer 2 (50 mM HEPES pH 7.5, 150 mM NaCl, 50 mM imidazole, 10% (vol/vol) glycerol, 0.025%/0.005% (wt/vol) DDM/CHS). The sample was eluted in 3.75 cv of elution buffer (50 mM HEPES pH 7.5, 150 mM NaCl, 250 mM imidazole pH 7.5, 10% (vol/vol) glycerol, 0.025%/0.005% (wt/vol) DDM/CHS) after discarding the first 0.6 cv of elution flow through, and subsequently concentrated to a volume of about 400 μl using an Amicon centrifugal filter with 100 kDa molecular weight cutoff (Millipore). The concentrated sample and 30 IU of His-tagged PSP (GenScript) were concomitantly passed over a PD MiniTrap G-25 desalting column (GE Healthcare) to remove imidazole and adjust detergent concentration to 0.05%/0.01% (wt/vol) DDM/CHS. After overnight incubation, cleaved tags and protease were removed by reverse IMAC, and the receptor was concentrated to ~20–30 mg ml^{-1} as above.

The receptor was reconstituted into lipidic cubic phase (LCP) by mixing two volumes of purified receptor with three volumes of molten monoolein/cholesterol (9:1 wt/wt) using coupled gas-tight 100 μl syringes (Hamilton) as previously described[44]. For initial crystallisation trials, protein-laden LCP boli (40 nl) were dispensed and overlaid with 800 nl of precipitant in 96-well glass sandwich plates (Marienfeld) using the NT8-LCP system (Formulatrix). Initial crystals of MT_1 bound to the high-affinity agonists ramelteon and 2-pmt were 30–50 μm size in the maximum dimension and could not be optimised to diffract better than 5 Å at a microfocus synchrotron beamline (Extended Data Fig. 1a, b). We then shifted our focus to obtaining small, high density crystals grown in syringes[45]. To prepare

samples for XFEL data collection, strings of 5 μl of protein-laden LCP were injected into syringes containing 50 μl of precipitant solution (60–100 mM potassium phosphate monobasic, 32–35% (vol/vol) PEG 400, 100 mM HEPES pH 7.0, 1 mM ligand, 2.5% (vol/vol) DMSO, 1.5% (vol/vol) propan-2-ol), and incubated for 3–10 days at 17 °C. After expulsion of excess precipitant, equivalent syringes were pooled together, and consolidated samples were reconstituted by addition of 7.9 MAG lipid[46].

Crystallographic data collection, structure solution and refinement.

Data were collected at the CXI instrument of the Linac Coherent Light Source (LCLS)[47] at photon energies of 9.52 and 9.83 keV, pulse duration of 30 and 43 fs, pulse repetition rate of 120 Hz, approximately 10^{11} photons per pulse (5–11% transmission), and beam size 1.5×1.5 μm^2. MT_1-CC micro-crystals (~5–10 μm size in maximum dimension, Extended Data Fig. 1c) were delivered at room temperature in a vacuum chamber to the intersection with the XFEL beam using an LCP jet viscous media injector[46] with a 50 μm nozzle at a flow rate of 0.3–0.36 μl min^{-1}, and diffraction images were collected using the CSPAD detector[48]. Crystal hits were identified by Cheetah[49] (more than 20 Bragg peaks of minimum 3 pixels in size with a signal-to-noise ratio better than 4 using an intensity threshold of 200 detector intensity units). Patterns were indexed, integrated, and merged with CrystFEL (v0.6.2)[50], using MOSFLM[51], DirAx[52], and XDS[53] for indexing with tightened tolerances of 1% on reciprocal unit cell dimensions and 0.5° on reciprocal unit cell angles. The total number of collected images/hits/indexed images are as follows: 517,530/43,306/42,679 (MT_1-CC-ramelteon), 726,497/119,563/99,897 (MT_1-CC-2-pmt), 429,006/21,776/21,038 (MT_1-CC-2-iodomelatonin), 466,602/45,820/43,423 (MT_1-CC-agomelatine). Integration radii of 3, 5, and 6 pixels with per pattern resolution cut-offs 1.2 nm^{-1} above the conservative resolution estimates for each crystal were used (*push-res* option). The default values were used for all other options. Based on apparent metric symmetry, data were first processed in a cubic space group, however, no molecular replacement solution could be found. A tetragonal lattice was then considered with the length of the unique axis *c* very close to that of the other two axes. This led to an indexing ambiguity where each crystal can be indexed in three different ways related by a permutation of the axes (*hkl* → *klh* → *lhk*). The correct assignment from the three options must be made for each crystal. Although the *ambigator* program implemented in CrystFEL can only distinguish between two possible indexing assignments at a time[54], in this case the threefold ambiguity could be resolved by applying the algorithm iteratively at least two times using the same axis permutation operator *hkl* → *klh*, which generates all three indexing options cyclically.

The structure of MT_1-CC-2-pmt was then solved by molecular replacement (MR) in space group P 4 2_1 2 using the backbone of the helical bundle of the human OX_2 orexin receptor[15] (PDB ID: 4S0V) as a search model, followed by a separate search against the PGS coordinates from the same structure using Phaser 2.1[55]. One copy of each molecule in the asymmetric unit were readily identified with TFZ scores (Z-score of the translation function) of 9.8 for both partial and final solution. The packing in our MT_1 crystals was found to be predominantly mediated by PGS, with the receptor crystallised as a monomer in the asymmetric unit, forming a layered structure with receptors from adjacent layers coordinated head to head (Extended Data Fig. 1f).

All refinements were performed with Refmac5[56] and Buster 2.10.2[57] followed by manual examination and rebuilding of the refined coordinates in the program Coot[58] using both $2mF_o-DF_c$ and mF_o-DF_c maps, as well as omit maps. Ligand restraints were generated by Prodrg[59]. The remaining three structures were solved by MR using the pruned protein coordinates of MT_1-CC-2-pmt as a search model, and repeating the refinement procedure described above. The Ramachandran plot determined by MolProbity[60] indicates that with the exception of Y79 of the YPYP motif all residues are in favoured/allowed regions: 97.1/2.7% of residues (MT_1-CC-ramelteon), 96/3.8% of residues in MT_1-CC-2-pmt, 96.4/3.4% of residues in MT_1-CC-2-iodomelatonin, 95.4/4.4% of residues in MT_1-CC-agomelatine. The final data collection and refinement statistics are shown in Extended Data Table 3. Simulated annealing omit maps (mF_o-DF_c) were calculated using Phenix[61].

Thermostability studies.

To assess the stability of solubilised receptor, 1–3 μg of purified protein were incubated in a volume of 100 μl at 4 °C for 20 minutes in the presence of 1.5 μM 7-diethylamino-3-(4-maleimidophenyl)-4-methylcoumarin (CPM, Sigma-Aldrich)[62], added as a stock solution in DMSO (1% final concentration, vol/vol), and 50 mM HEPES pH 7.5, 150 mM NaCl, 10% (vol/vol) glycerol, and 0.05%/0.01% (wt/vol) DDM/CHS. After incubation of the sample at room temperature for 5 minutes, thermal unfolding of the receptor was induced and monitored using a Rotor-Gene Q instrument (QIAGEN) between 25 to 95 degrees (+2 °C min^{-1}) at wavelengths 365 nm (excitation) and 460 nm (emission), and gain settings of −2 to −1, and melting temperatures were extracted from the first derivative of the melting curve.

Synthesis of bitopic compound.

N-{2-[7-(2-{2-[8-(2-Acetylaminoethyl)-naphthalen-2-yloxy]-ethoxy}-ethoxy)-naphthalen-1-yl]-ethyl}acetamide (Compound **2**, CTL 01–05-B-A05) was obtained in one step by condensation of the described[63] *N*-[2-(7-hydroxynaphth-1-yl)ethyl]acetamide (**1**) with bis(2-bromoethyl)ether in the presence of potassium carbonate in acetonitrile[64]. Synthesis scheme, experimental section, and NMR-spectra are shown in Supplementary Figures 7 and 8.

Radioligand Binding Assays.

Binding assays were performed using HEK293T cells (purchased from ATCC, CRL-11268, authenticated by supplier using morphology, growth characteristics and STR profiling, certified mycoplasma-free) transfected with wild-type or mutants of MT_1. All binding assays were performed in standard binding buffer (50 mM Tris, 10 mM $MgCl_2$, 0.1 mM EDTA, 0.1% BSA, 0.01% ascorbic acid, pH 7.4) using [^{3}H]-melatonin (PerkinElmer, specific activity = 77.4–84.7 Ci/mmol) as the radioligand. For competitive binding, assays were performed with various concentrations of cold unlabeled ligands (100 fM to 10 μM), [^{3}H]-melatonin (0.2–1.7 nM), and resuspended membranes in a total volume of 125 μL. Competition assays were incubated for 4 hours at 37 °C in a humidified incubator until harvesting. For constructs with reduced binding affinity for [^{3}H]-melatonin, homologous competition binding assays were carried out at two [^{3}H]-melatonin concentrations (about 1–2 and 5–10 nM) to estimate K_d values. For all assays, non-specific activity was defined as the addition of 5 μM 2-pmt. For determining the effect of NaCl on melatonin binding

affinity, 147 mM NaCl was included in the binding buffer. Plates were harvested using vacuum filtration onto 0.3% polyethyleneimine pre-soaked 96 well Filtermat A (PerkinElmer) and washed three times with 250 μl per well of cold wash buffer (50 mM Tris, pH 7.4). Filters were dried and scintillation cocktail (Meltilex, PerkinElmer) was melted and allowed to cool to room temperature. Afterwards, filter plates were placed in cassettes and read using a Wallac TriLux Microbeta counter (PerkinElmer). Data were analysed either using "One-site-homologous" (to yield K_d) or "One-site-Fit K_i" (to yield K_i) using GraphPad Prism 5.0.

MT_1 Gi/o-mediated cAMP inhibition Assay.

MT_1 Gi/o-mediated cAMP inhibition assays were performed in HEK293T cells (ATCC CRL-11268, mycoplasma-free) co-expressing the cAMP biosensor GloSensor-22F (Promega) and human MT_1. Transfected cells were seeded (10–15,000 cells/40 μl/well) into poly-L-lysine coated white 384 clear-bottom, tissue culture plates in DMEM containing 1% dialysed FBS. Next day, ligands were diluted from 10 μM to 100 fmol in HBSS (Hank's Balanced Salt Solution), 20 mM HEPES, 0.1% BSA, 0.01% ascorbic acid, pH 7.4. Media was removed on 384 well plates and 20 μl of drug buffer (HBSS, 20 mM HEPES, pH 7.4) was added per well and allowed to equilibrate for at least 15 minutes at room temperature. To start the assay, cells were treated with 5 μl per well of 5× concentrated ligands in HBSS, 20 mM HEPES, 0.1% BSA, 0.01% ascorbic acid, pH 7.4 using a FLIPR (Molecular Devices). After 15 min, cAMP accumulation was initiated by addition of 10 μl/well of 0.3 μM isoproterenol (final concentration) in GloSensor reagent. Luminescence per well per second (LCPS) was read on a Wallac TriLux Microbeta counter (PerkinElmer). Data were normalised to maximum cAMP inhibition by melatonin (100%) and basal cAMP accumulation by isoproterenol (0%), and analysed using the sigmoidal dose-response function in GraphPad Prism 5.0.

Transmembrane segment sequence analysis.

To analyse amino acid frequencies and distributions in transmembrane segments, two datasets were constructed: one dataset comprising experimentally determined, representative structures of membrane proteins (*experimental-TM*); and one dataset comprising the subset of the human proteome with transmembrane regions predicted by a computational method (*human-TM*).

The *experimental-TM* dataset was constructed as follows: A list of experimental polypeptide X-ray structures was retrieved from the OPM database[65] which provides quaternary assemblies and membrane boundaries for all experimental membrane protein structures from the Protein Data Bank[66]. Because OPM also contains non-helical proteins (e.g. β-barrel folds) that would skew our analysis, only entries containing at least one helical membrane spanning element were retained. To this end, the secondary structure of each polypeptide chain was computed using DSSP[67] v3.0, and for each annotated TM segment that was determined to be at least 80% helical, leading and trailing non-helical residues were removed. After removing one more residue from either side so as to minimise contamination by flanking regions, segments longer than 17 amino acids were retained. Next, for duplicate polypeptide chains only those with highest resolution were retained. The unique chains were

clustered hierarchically using single linkage clustering as implemented in the *treecluster* routine of Biopython[68]. When extracting amino acid sequences only residues with a residue numbering between 1 and 999 were retained to eliminate expression tags and soluble GPCR fusion partners. Distances were calculated from global sequence alignments for each pair of sequences, using the *pairwise2* routine of Biopython with gap open and extension penalties of −10 and −0.5 and the BLOSUM62 substitution matrix[69]. Gaps at alignment ends were not penalised, and sequence identity (in %) was calculated over all experimentally observed residues and converted to distance as 1-identity/100%. The “tree” resulting from the clustering was cut and clades collapsed to clusters with representative polypeptide chains chosen from each cluster such that a) cluster representatives have the minimum average distance to all other entries in the same cluster, and b) cluster representatives are at most 95% identical to each other. The cluster representatives then form a balanced dataset of 2,965 TM segments in 741 polypeptide chains and 546 PDB entries with reduced sequence bias.

To construct the *human-TM* dataset, 20,245 reference sequences representing the human proteome were downloaded from UniProt[33] and submitted to the TMHMM Server v2.0[70] to computationally predict TM segments. This analysis identified 5,225 proteins with at least one TM segment of no less than 18 amino acids, 2,286 of which were single pass proteins, and 18,959 such TM segments overall.

The observed amino acid frequencies in the TM segments of the two datasets were compared to their expected frequencies, which were calculated by shuffling the primary sequence of each protein in the dataset, and counting the occurrence of a given amino acid in a fraction of the length of that randomised sequence that corresponds to the experimentally determined or computationally predicted TM content (see above). Statistics were accumulated per dataset by shuffling each protein sequence 10,000 times, with the average count for a given amino acid approximating its expected value. Despite amino acid counts being discrete, they were found to be sufficiently well represented by a normal distribution, as manually inspected by quantile-quantile plots. Significance was estimated by comparing the observed count with the sample mean of the distribution of 10,000 randomised counts and integrating over the two more extreme tails of this distribution. Similarly, patterns of consecutive amino acids were analysed in both datasets following the outline of an earlier study[71]. Observed counts for patterns in TM segments were compared to expected counts given the distribution of individual amino acids in TM segments, i.e. instead of randomising the entire protein sequence as above, only amino acids within TM segments were shuffled, and instances of a given pattern were counted in this randomised set of (independent) TM segments. Statistics were accumulated and p-values estimated as above.

We analysed the two datasets for the occurrence of the YPYP motif and, given the significantly lower abundance of proline residues in TM segments (observed fraction 0.51–0.66 of their expected number in human proteome and PDB, respectively, $p<0.0001$), found this motif occurring in melatonin receptors to be statistically significant ($p<0.025$), and not to exist in receptors other than the melatonin receptors.

Cheminformatics.

Ligand datasets for a given receptor, identified by its UniProt[33] accession, were retrieved from ChEMBL24[23], and limited to data points with available binding ("B") data. Affinities were converted to pK_i, and for ligands with multiple reported affinity values pK_i values were averaged. Substructure searches and matching were performed with rdkit (http://www.rdkit.org), and ligand protonation states estimated with OpenBabel[72] at pH 7.4.

Channel diameter determination.

Channel dimensions were obtained using the CAVER analyst v2.0[73]. After addition of hydrogens to the coordinates of the MT_1-ramelteon crystal structure using PyMOL[74], a tunnel starting point was placed manually close to the perceived channel entrance. Using default program parameters, channel dimensions were extracted and trimmed to the segment between the channel entrance and ligand centroid. The residue proximity matrix was calculated for pore-lining residues within 5 Å of the respective probe position, with distances calculated as minima to any residue atom including hydrogens.

Molecular docking.

MT_1 ligands obtained from the ChEMBL database[23] were docked into the ramelteon-bound crystal structure using an energy-based docking in ICM-Pro v3.8–6[75]. Receptor structures were optimised using the ICM docking protocols. Ligands selected for docking were converted from chemical structures to optimise their three-dimensional geometry and charges according to the MMFF force field[76]. Docking grid maps were generated using the receptor model, and ligands were docked using Biased Probability Monte Carlo (BPMC) sampling and optimisation method with conformational sampling thoroughness of 50, starting with random initial ligand conformations. At least 5 independent runs were performed for the docking of the ligand set, and consistent dock poses were selected for further interaction analysis. The docking protocol did not use distance restraints or any other *a priori* derived information to guide ligand-receptor interactions. The same procedure was applied to dock agomelatine to the 5-HT_{2C} structure[31] (PDB ID: 6BQG).

Molecular dynamics simulation.

The experimental structure of MT_1 was pre-processed to assign protonation states and to model missing side chains using ICMFF energy-based optimisation protocols available in the ICM-Pro molecular modelling package[75] (v3.8–6). The missing ICL3 coordinates were modeled using *Loop modelling* and *Regularization* protocols in ICM-Pro. The pre-processed structure was subjected to molecular dynamics simulation as previously described[77], using input files generated by the CHARMM-GUI web-server[78]. For initial membrane embedding, the MT_1 models were superimposed to the 5-HT_{2B} (PDB ID: 4NC3) receptor structure[79] retrieved from the OPM database[65]. The structure was simulated in a periodic box with dimensions (x, y, z) 75.5 Å, 75.5 Å, 105.4 Å, containing lipids (129 copies of the POPC lipid), 10,284 water molecules, 27 sodium, and 41 chloride ions. Parameters for melatonin and 2-pmt were obtained using CGenFF[80] available with the CHARMM-GUI server. After the initial energy minimisation, the system was equilibrated for 10 ns, followed by production runs of up to 1 μs.

Membrane boundaries were derived as follows: for a set of 1,000 snapshots evenly spaced in time across the 1 μs trajectory, coordinates were superimposed to the crystal structure reference to eliminate receptor motion, the membrane being oriented along the x-y plane. Then, the positions of the carbonyl oxygen atoms of POPC molecules furthest from the lipid head groups were used to represent the boundaries of the hydrophobic slab. For each snapshot, this yields a set of 129 oxygen atom coordinates, 64 (65) of which represent the upper (lower) leaf of the bilayer. Next, two planes were fit to these coordinates, representing the upper and lower membrane boundary, respectively, using a least-squares method, minimising vertical (z-coordinate) distance of the points to the plane. The parameters of the resulting pair of planes were used to determine statistics over the course of the simulation, such as bilayer thickness and buriedness of the lateral ligand access channel below the extracellular membrane leaf, the position of which was defined as the mid-point between the smallest and largest z-coordinate of the side chains of channel-lining receptor residues $Y187^{5.38}$ and $H195^{5.46}$, respectively. This channel coordinate was found to fluctuate very little over the course of the simulation (s.d. = 0.4 Å). The channel entrance was found to lie 6.5 to 10.9 Å below the upper boundary of the hydrophobic slab (values from quartiles of the distance distribution; mean 8.7±3.4 Å s.d., median 8.8 Å), and the average thickness of the hydrophobic slab was 30.0 Å±1.7 Å.

Data availability

Coordinates and structure factors were deposited in the Protein Data Bank (PDB) under the following accession codes: 6ME2 (MT_1-CC-ramelteon), 6ME3 (MT_1-CC-2-pmt), 6ME4 (MT_1-CC-2-iodomelatonin), and 6ME5 (MT_1-CC-agomelatine).

Extended Data

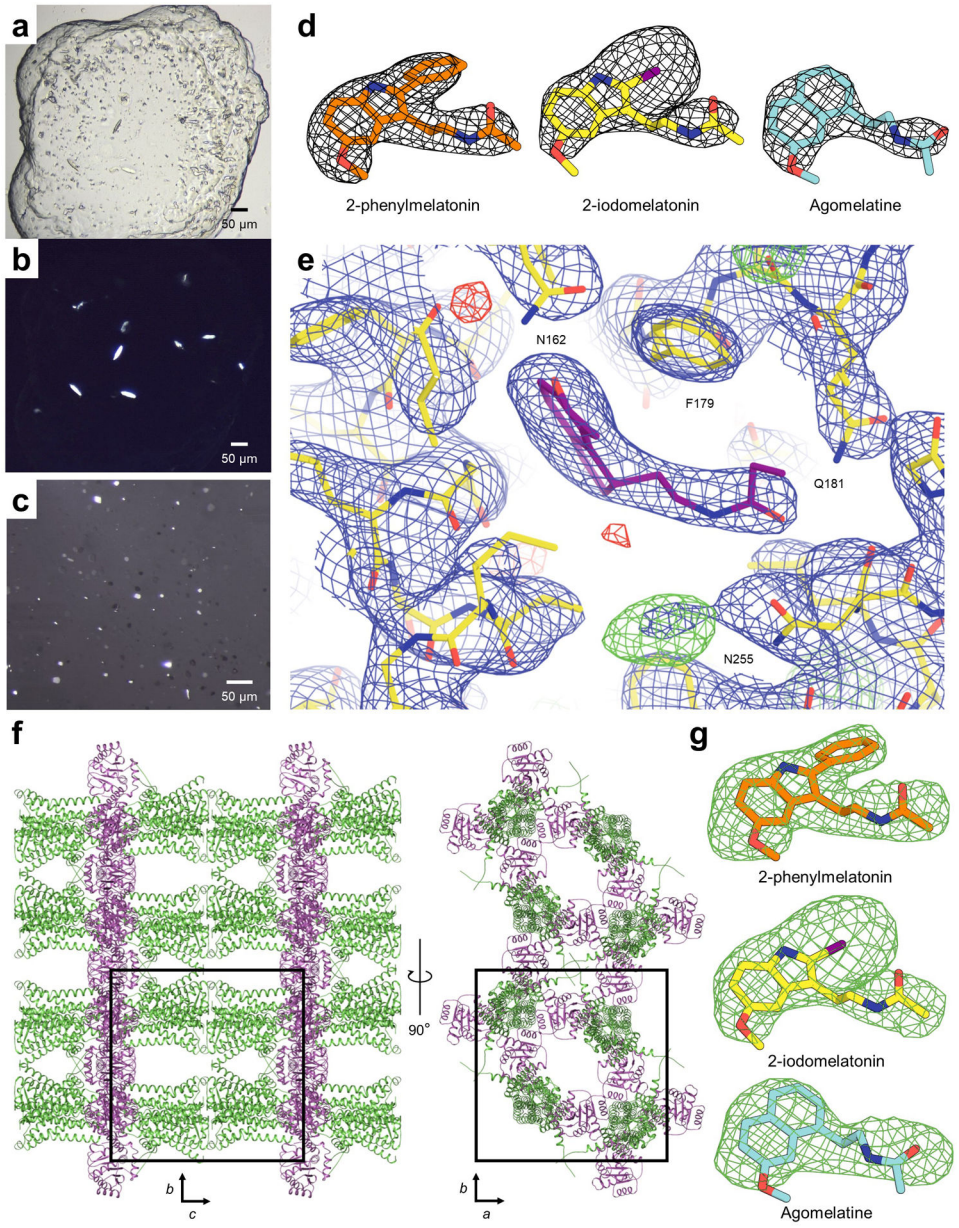

Extended Data Fig. 1 |. Crystals, ligand electron density maps, and packing of MT_1.
a, Bright field, and **b**, cross-polarised images of representative MT_1-2-pmt crystals, optimised for synchrotron data collection (representing three independent crystallization setups). **c**, Cross-polarised image of representative MT_1-ramelteon crystals used for XFEL data collection (representing two independent crystallization setups). **d**, $2mF_o-DF_c$ ligand electron density maps of MT_1 co-crystallised with 2-pmt (orange), 2-iodomelatonin (yellow), and agomelatine (cyan), contoured at 1.0 σ (grey mesh). **e**, $2mF_o-DF_c$ (blue, contoured at 1.0 σ) and mF_o-DF_c (green/red, +/−3.5 σ) electron density maps of MT_1-ramelteon (ligand purple, protein yellow) illustrating the small, unassigned electron density close to $N255^{6.52}$ that is tentatively attributed to the essential additive 2-propan-ol. The distance from this electron density to the closest ligand atom is approximately 4.8 Å. **f**,

Packing of MT_1-PGS crystallised in the P 4 2_1 2 space group. The receptor is shown in green and the PGS fusion protein is shown in purple. **g**, Simulated annealing mF_o-DF_c omit maps (green mesh) of 2-pmt (orange sticks), 2-iodomelatonin (yellow), and agomelatine (cyan), contoured at 3.0 σ.

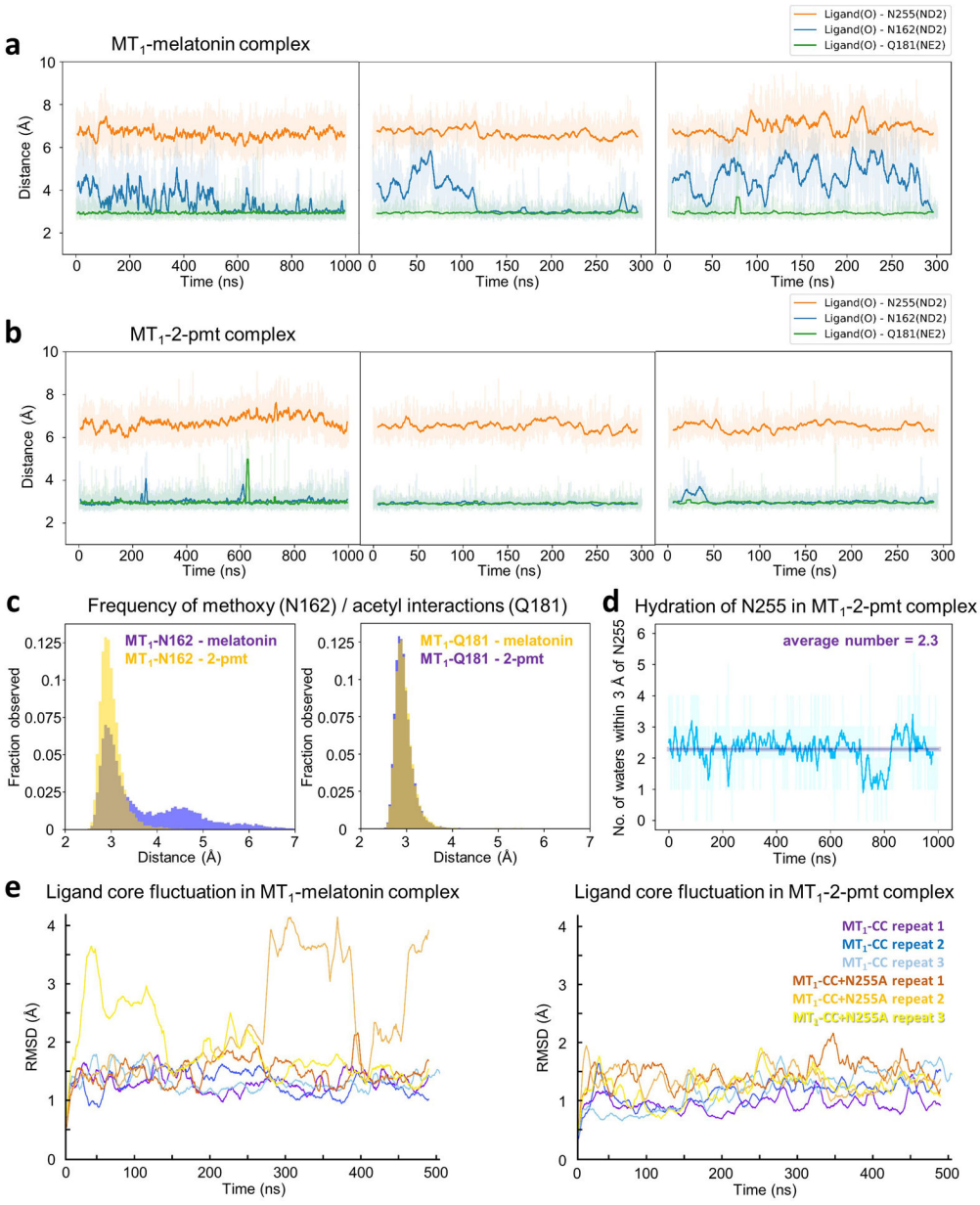

Extended Data Fig. 2 |. Molecular dynamics simulations.

a, b, Distance plots for interactions between residues in MT_1 ($N162^{4.60}$, atom type ND2 (N^{δ}); $Q181^{ECL2}$, atom NE2 (N^{ε}); $N255^{6.52}$, atom ND2), and closest oxygen atoms of the methoxy and acetyl groups, respectively, in ligands melatonin (**a**) and 2-pmt (**b**) from three independent simulation runs. **c**, Distance histograms for interactions of methoxy with N162 (left), and Q181 with ligand acetyl tail (right), in melatonin and 2-pmt complexes. **d**, Hydration of residue $N255^{6.52}$ over the course of a 1 μs simulation of the MT_1-2-pmt complex from three independent simulations. **e**, Stability of ligand binding in simulations of MT_1 complexes. Time dependence of RMSD for non-hydrogen atoms of melatonin shown for MT_1-melatonin complex (left) and MT_1-2-pmt complex (right). Three independent simulations of crystal construct (purple, blue, light blue) and crystal construct with

N255$^{6.52}$A mutation (orange, light orange, yellow) are shown, spanning 1.5 μs of cumulative time per system. Sampling rate was 10 frames per ns, and solid lines represent moving average values from 50 frames in all cases.

Extended Data Table 1 | MT1 radioligand affinity.

Affinity was determined using radioligand competition binding and [^{3}H]-melatonin to yield K_d or K_i affinity estimates (number of independent experiments in square brackets) for wild-type (WT) and mutants expressed in HEK293T cells. MT_1-CC, crystal construct (including PGS fusion) expressed in Sf9 cells; MT_1-9mut, construct combining all crystallogenic mutations, expressed in HEK293T. MT_1-PGS, wild-type construct with PGS fusion. ND, not determined. Binding isotherms are shown in Supplementary Figure 1. For determining the effect of NaCl, binding assays were performed in the presence of 147 mM NaCl (binding isotherms in Supplementary Figure 2).

	melatonin	2-pmt	ramelteon	agomelatine	2-iodomelatonin
	K_d, nM [n] (pK_d ± s.e.m.)	K_i, nM [n] (pK_i ± s.e.m.)	K_i, nM [n] (pK_i ± s.e.m.)	K_i, nM [n] (pK_i ± s.e.m.)	K_i, nM [n] (pK_i ± s.e.m.)
WT	0.85 [11] (9.07±0.13)	0.42 [3] (9.46±0.18)	0.43 [4] (9.45±0.18)	1.67 [3] (8.79±0.08)	0.12 [3] (9.92±0.07)
WT + NaCl	2.46 [6] (8.61±0.11)	ND	ND	ND	ND
MT_1-CC (Sf9)	36.0 [7] (7.44±0.07)	7.41 [6] (8.13±0.09)	18.2 [3] (7.74±0.15)	29.5 [3] (7.53±0.01)	15.5 [3] (7.81±0.06)
MT_1-CC (Sf9) + NaCl	34.3 [5] (7.46±0.07)	ND	ND	ND	ND
MT_1-9mut	44.7 [7] (7.35±0.05)	9.70 [3] (8.01±0.24)	2.97 [3] (8.53±0.02)	14.9 [3] (7.83±0.04)	ND
MT_1-9mut + NaCl	32.4 [5] (7.49±0.03)	ND	ND	ND	ND
MT_1-PGS	1.62 [3] (8.79±0.05)	0.16 [4] (9.79±0.03)	ND	ND	ND
D73N (2.50)	195.0 [3] (6.71±0.06)	5.45 [3] (8.26±0.20)	ND	ND	ND
L95F (ECL1)	1.42 [3] (8.85±0.01)	0.24 [3] (9.63±0.10)	ND	ND	ND
G104A (3.29)	0.86 [3] (9.07±0.07)	0.12 [3] (9.91±0.08)	ND	ND	ND
F116W (3.41)	2.42 [3] (8.62±0.05)	0.37 [3] (9.43±0.06)	ND	ND	ND
N124D (3.49)	0.76 [3] (9.12±0.04)	0.09 [3] (10.03±0.12)	ND	ND	ND
C127L (3.52)	0.10 [3] (9.98±0.05)	0.04 [3] (10.40±0.03)	ND	ND	ND
W251F (6.48)	2.88 [3] (8.54±0.09)	0.06 [3] (10.23±0.17)	ND	ND	ND
A292P (7.50)	4.90 [3] (8.31±0.00)	1.27 [3] (8.90±0.07)	ND	ND	ND
N299D (8.47)	8.38 [3] (8.08±0.24)	3.29 [3] (8.48±0.21)	ND	ND	ND
H99A (3.24)	2.82 [3] (8.55±0.07)	0.28 [3] (9.55±0.05)	ND	ND	ND

	melatonin	2-pmt	ramelteon	agomelatine	2-iodomelatonin
	K_d, nM [n] (pK_d ± s.e.m.)	K_i, nM [n] (pK_i ± s.e.m.)	K_i, nM [n] (pK_i ± s.e.m.)	K_i, nM [n] (pK_i ± s.e.m.)	K_i, nM [n] (pK_i ± s.e.m.)
N162A (4.60)	1.45 [3] (8.85±0.06)	0.20 [3] (9.71±0.06)	0.10 [3] (10.00±0.08)	0.74 [3] (9.14±0.07)	ND
F179A (ECL2)	*no specific binding up to 7 nM of radioligand*				
Q181A (ECL2)	1.80 [3] (8.85±0.23)	0.44 [3] (9.42±0.16)	0.36 [3] (9.58±0.26)	1.19 [3] (8.97±0.10)	ND
Q181E (ECL2)	1.85 [3] (8.73±0.03)	0.24 [3] (9.63±0.04)	0.28 [3] (9.57±0.10)	2.80 [3] (8.58±0.11)	ND
N255A (6.52)	2.04 [3] (8.79±0.25)	0.29 [3] (9.55±0.06)	0.43 [3] (9.39±0.11)	2.42 [3] (8.67±0.16)	ND
H195A (5.46)	*low expression / no specific binding up to 7 nM of radioligand*				
M107A (3.32)	0.65 [3] (9.23±0.14)	0.054 [3] (10.29±0.10)	0.08 [3] (10.15±0.13)	0.14 [3] (9.85±0.04)	ND

Extended Data Table 2 | Functional data (Gi/o Glosensor) for crystallogenic mutants.

Data were acquired with MT_1 wild-type (WT) and crystallogenic mutants by using GloSensor to measure Gi/o-mediated cAMP inhibition via isoproterenol stimulation. Data represent means of EC_{50} (number of independent experiments in square brackets), represented as mean pEC_{50} ± s.e.m. as well as E_{MAX} shown as mean $\%E_{MAX}$ ± s.e.m. %Emax is relative to wild-type receptor in columns, and (%Emax*) is relative to melatonin in rows. Mutant effects were calculated by the change in relative activity, or log(E_{MAX} / EC_{50}) subtracting wild-type from mutant. MT_1-PGS, wild-type construct with PGS fusion. MT_1-9mut, construct combining all nine crystallogenic mutations. MT_1-PGS, wild-type construct with PGS fusion. Dose-response curves are shown in Supplementary Figure 3.

	melatonin			2-pmt		
	EC_{50}, nM [n] (pEC_{50})	% E_{MAX} (% E_{MAX}*)	Δlog(E_{MAX} / EC_{50})	EC_{50}, nM [n] (pEC_{50})	% E_{MAX} (% E_{MAX}*)	Δlog(E_{MAX} / EC_{50})
WT	0.0045 [23] (11.34±0.07)	100 (100)	0	0.0047 [16] (11.32±0.13)	100 (107±3)	**0**
MT_1-PGS	0.50 [12] (9.30±0.14)	42±2 (100)	−2.42	0.22 [12] (9.65±0.13)	39±2 (100±8)	−2.09
D73N (2.50)	11.78 [10] (7.93±0.07)	106±4 (100)	−3.39	0.5860 [10] (9.23±0.19)	110±3 (111±3)	−2.05
L95F (ECL1)	0.0042 [10] (11.37±0.23)	89±7 (100)	−0.02	0.0033 [6] (11.48±0.31)	92±5 (110±6)	+0.12
G104A (3.29)	0.0058 [7] (11.24±0.14)	100±4 (100)	−0.11	0.0046 [6] (11.34±0.19)	100±3 (107±3)	+0.02
F116W (3.41)	0.0069 [8] (11.16±0.13)	108±5 (100)	−0.15	0.0031 [7] (11.51±0.13)	103±3 (102±3)	+0.20
N124D (3.49)	0.0405 [7] (10.39±0.12)	104±9 (100)	−0.93	0.0068 [6] (11.17±0.14)	110±3 (117±3)	−0.11
C127L (3.52)	0.0111 [7] (10.95±0.19)	105±11 (100)	−0.37	0.0044 [6] (11.36±0.12)	115±5 (116±5)	+0.09

	melatonin			2-pmt		
	EC_{50}, nM [n] (pEC_{50})	**% E_{MAX} (% E_{MAX}*)**	**Δlog(E_{MAX} / EC_{50})**	**EC_{50}, nM [n] (pEC_{50})**	**% E_{MAX} (% E_{MAX}*)**	**Δlog(E_{MAX} / EC_{50})**
W251F (6.48)	0.0603 [7] (10.22±0.11)	99±7 (100)	−1.13	0.0041 [6] (11.38±0.11)	95±5 (104±5)	+0.04
A292P (7.50)	0.0187 [7] (10.73±0.07)	114+6 (100)	−0.56	0.0030 [6] (11.52±0.16)	111+5 (105±5)	+0.24
N299D (8.47)	0.0644 [7] (10.19±0.12)	107±4 (100)	−1.12	0.0299 [6] (10.53±0.20)	98±5 (100±5)	−0.81
MT_1-9mut	*no activity*					

Extended Data Table 3 | MT1 Crystallographic data collection and refinement statistics.

	MT_1-CC-ramelteon[a]	**MT_1-CC-2-pmt[b]**	**MT_1-CC-2-iodomelatonin[c]**	**MT_1-CC-agomelatine[d]**
Data collection				
Space group	P4 2_1 2	P4 2_1 2	P4 2_1 2	P4 2_1 2
Cell dimensions				
a, *b*, *c* (Å)	122.3, 122.3, 122.8	122.4, 122.4,122.8	122.6, 122.6, 123.3	122.2, 122.2,122.8
α, β, γ (°)	90, 90, 90	90, 90, 90	90, 90, 90	90, 90, 90
Resolution (Å)	29.7–2.80 (2.92–2.80)	30.6–2.90 (3.04–2.90)	28.9–3.20 (3.42–3.20)	28.9–3.20 (3.42–3.20)
R_{split}	0.100 (3.56)	0.098 (2.96)	0.150 (2.10)	0.120 (1.67)
$I/\sigma I$	7.9 (0.33)	9.4 (0.39)	6.5 (0.57)	8.7 (0.70)
$CC_{1/2}$ (%)	99.93 (56.0)	99.95 (54.5)	99.87 (60.4)	99.85 (54.5)
Completeness (%)	100 (100)	100 (100)	100 (100)	100 (100)
Redundancy	1,003 (187.4)	2,323 (489.3)	595 (85.8)	1,131 (151.6)
Refinement				
Resolution (Å)	29.67–2.80	30.00–2.90	28.91–3.20	28.87–3.20
No. reflections	23,262	21,300	15,957	15,853
R_{work}/R_{free}	0.204/0.230	0.203/0.229	0.209/0.249	0.232/0.257
No. atoms				
Protein	3,738	3,753	3,702	3,668
Ligand	19	23	18	18
Lipid and other	40	19	16	9
B-factors ($Å^2$)				
Receptor	114.4	113.4	133.0	117.9
PGS	104.1	99.7	124.5	109.7
Ligand	101.9	94.3	126.4	105.3
Lipids and other	107.8	106.9	118.5	110.0
R.m.s. deviations				
Bond lengths (Å)	0.008	0.009	0.009	0.009
Bond angles (°)	0.94	0.98	0.95	0.93

Footnote: Number of crystals used for structure determination: a46,679, b99,897, c21,038, and d42,423. Values in parentheses are for highest-resolution shell.

Extended Data Table 4 | Volumes of enclosed binding sites of class A GPCRs.

receptor	PDB ID	ligand	Volume, Å^3
MT_1	6ME2	ramelteon	710
MT_1	6ME3	2-pmt	710
MT_1	6ME4	2-iodomelatonin	714
MT_1	6ME5	agomelatine	702
CB_1	5XRA	CHEMBL1683648	928
CB_1	5U09	taranabant	1043
$S1P_1$	3V2W	sphingosine mimetic	936
FFA_1	5TZR	MK-8666	378 *
LPA_1	4Z35	ONO-9910539	904
rhodopsin (active)	2X72	all-*trans* retinal	894
rhodopsin (inactive)	1U19	11-*cis* retinal	598

Footnote:
* large part of ligand is outside binding pocket.

Extended Data Table 5 | Thermostability data.

Melting temperature (T_m, mean ± s.d. for n=3 independent experiments) for crystallised construct (MT_1-CC) and several of its mutants purified in absence (apo) and presence (100 μM) of ligand (mlt, melatonin; 2-pmt, 2-phenylmelatonin; rmt, ramelteon). ND, not determined. Melting curves are shown in Supplementary Figure 4.

Mutant	apo T_m, °C	mlt T_m, °C	2-pmt T_m, °C	rmt, T_m, °C	mlt ΔT_m, °C	2-pmt ΔT_m, °C	rmt ΔT_m, °C
MTi-CC	59.4±0.5	67.3±0.3	75.6+0.1	73.9±0.2	+7.9	+16.2	+14.5
N162A (4.60)	59.9±0.8	67.1±0.8	ND	73.3±0.8	+7.2	ND	+13.4
F179A (ECL2)	55.1±0.6	55.2±0.5	ND	59.9±0.1	+0.1	ND	+4.8
Q181A (ECL2)	60.8±0.4	65.0±0.2	72.6+0.1	74.0±0.4	+4.2	+11.8	+13.2
N255A (6.52)	59.6±0.6	60.3±0.4	66.8+0.3	64.6±0.4	+0.7	+7.2	+5.0
Q181A/N255A	61.7±0.2	62.1±0.4	ND	64.9±0.4	+0.4	ND	+3.2
M107A (3.32)	55.3±1.1	62.8±0.8	ND	69.4±1.0	+7.5	ND	+14.1
M107D (3.32)	ND	61.7±0.3	ND	67.9±0.6	ND	ND	ND
G108A (3.33)	60.8±0.5	61.0±0.6	ND	65.0±0.1	+0.2	ND	+4.2
F194A (5.45)	57.9±0.2	65.6±0.1	ND	73.3±0.3	+7.7	ND	+15.4
H195A (5.46)	56.7±1.5	66.2±0.2	ND	71.8±0.2	+9.5	ND	+15.1
F196A (5.47)	52.9±0.1	58.2±0.3	ND	66.5±0.1	+5.3	ND	+13.6
Y79A (2.56)	ND	55.7±0.5	ND	63.3±0.7	ND	ND	ND
Y79F (2.56)	ND	61.0±0.1	ND	68.6±0.2	ND	ND	ND
P80A (2.57)	ND	59.8±0.8	ND	67.2±0.8	ND	ND	ND
Y81A (2.58)	ND	60.3±0.1	ND	67.4±0.5	ND	ND	ND
Y81F (2.58)	55.8±0.1	65.3±0.1	ND	72.5±0.1	+9.6	ND	+16.8

Mutant	apo T_m, °C	mlt T_m, °C	2-pmt T_m, °C	rmt, T_m, °C	mlt ΔT_m, °C	2-pmt ΔT_m, °C	rmt ΔT_m, °C
P82A (2.59)	ND	57.8±0.2	ND	65.1±0.4	ND	ND	ND
H99L (3.24)	ND	59.7±0.1	ND	67.9±0.2	ND	ND	ND

Extended Data Table 6 |

Functional data (Gi/o GloSensor) for mutants of the YPYP motif and the ligand binding site.

Data were acquired with MT_1 wild-type (WT) and mutants by using GloSensor to measure Gi/o-mediated cAMP inhibition via isoproterenol stimulation. Data represent means of EC_{50} (number of independent experiments in square brackets), shown as mean(pEC_{50}) ± s.e.m. as well as E_{MAX} shown as mean($\%E_{MAX}$) ± s.e.m. $\%E_{MAX}$ is relative to wild-type receptor in columns, and ($\%E_{MAX}$*) is relative to melatonin in rows. Mutant effects were calculated by the change in relative activity, or log(E_{MAX} /EC_{50}) subtracting wild-type from mutant. ND, not determined. Dose-response curves are shown in Supplementary Figure 5.

	melatonin			**2-pmt**			**ramelteon**			**agomelatine**		
	EC_{50}, nM [n] (pEC_{50})	**$\%E_{MAX}$ ($\%E_{MAX}$*)**	**Δlog (E_{MAX}/ EC_{50})**	**EC_{50}, nM [n] (pEC_{50})**	**$\%E_{MAX}$ ($\%E_{MAX}$*)**	**Δlog (E_{MAX}/ EC_{50})**	**EC_{50}, nM [n] (PEC_{50})**	**$\%E_{MAX}$ ($\%E_{MAX}$*)**	**Δlog (E_{MAX}/ EC_{50})**	**EC_{50}, nM [n] (pEC_{50})**	**$\%E_{MAX}$ ($\%E_{MAX}$*)**	**Δlog (E_{MAX}/ EC_{50})**
WT	0.0045 [23] (11.34±0.07)	100 (100)	0	0.0047 [16] (11.32±0.13)	100 (107±3)	0	0.0035 [12] (11.45±0.15)	100 (98±3)	0	0.0084 [10] (11.07±0.11)	100 (107±5)	---
Y79A (2.56)	0.2380 [4] (9.62±0.14)	121±17 (100)	−1.64	0.0166 [4] (10.78±0.10)	81 ±2 (71±1)	−0.64	0.0339 [4] (10.47±0.09)	88±2 (71±1)	−1.04	2.3988 [4] (8.62±0.09)	81±2 (71±1)	−2.55
Y79F (2.56)	0.0537 [4] (10.27±0.08)	98±2 (100)	−1.08	0.0052 [4] (11.28±0.07)	92±2 (100±2)	−0.08	0.0060 [4] (11.22±0.07)	100±2 (100±2)	−0.23	0.3802 [4] (9.42±0.07)	92±2 (100±2)	−1.69
P80A (2.57)	0.3020 [4] (9.52±0.10)	79±2 (100)	−1.92	0.0316 [4] (10.50±0.09)	74±2 (100±2)	−0.95	0.0251 [4] (10.60±0.08)	81±2 (100±2)	−0.95	0.3715 [4] (9.43±0.10)	74±2 (100±2)	−1.77
Y81A (2.58)	0.0347 [4] (10.46±0.17)	107±2 (100)	−0.85	0.0012 [4] (11.91±0.06)	100±2 (100±2)	+0.59	0.0048 [4] (11.32±0.06)	109±2 (100±2)	−0.10	0.0891 [4] (10.05±0.07)	100±2 (100±2)	−1.02
P82A (2.59)	0.1514 [4] (9.82± 0.06)	57±2 (100)	−1.77	0.0269 [4] (10.57±0.10)	53±2 (100±3)	−1.03	0.0575 [4] (10.24±0.10)	58±2 (100±3)	−1.45	0.2042 [4] (9.69±0.12)	53±2 (100±3)	−1.66
H99A (3.24)	0.0034 [4] (11.47±0.08)	91±2 (100)	+0.09	0.0014 [4] (11.85±0.09)	86±2 (100±2)	+0.46	0.0011 [4] (11.96±0.11)	93±2 (100±2)	+0.48	0.0040 [4] (11.40±0.10)	85±2 (100±2)	+0.26
N162A (4.60)	*no activity*											
F179A (ECL2)	5957 [5] (5.23±0.07)	124±2 (100)	−6.02	748 [5] (6.13±0.05)	118±0 (96±3)	−5.12	501 [5] (6.30±0.08)	125±2 (89±4)	−5.06	1159 [5] (5.94±0.11)	118±2 (97±3)	−5.06
Q181A (ECL2)	*no activity*											

	melatonin			2-pmt			ramelteon			agomelatine		
	EC_{50}, nM [n] (pEC_{50})	**$\%E_{MAX}$ ($\%E_{MAX}$*)**	**Δlog (E_{MAX}/ EC_{50})**	**EC_{50}, nM [n] (pEC_{50})**	**$\%E_{MAX}$ ($\%E_{MAX}$*)**	**Δlog (E_{MAX}/ EC_{50})**	**EC_{50}, nM [n] (PEC_{50})**	**$\%E_{MAX}$ ($\%E_{MAX}$*)**	**Δlog (E_{MAX}/ EC_{50})**	**EC_{50}, nM [n] (pEC_{50})**	**$\%E_{MAX}$ ($\%E_{MAX}$*)**	**Δlog (E_{MAX}/ EC_{50})**
Q181E (ECL2)	1.2882 [5] (8.89±0.07)	131±2 (100)	−2.34	0.0461 [5] (10.34±0.09)	116±3 (95±3)	−0.92	0.4831 [5] (9.32±0.08)	123±4 (92±3)	−2.05	5.3951 [5] (8.27±0.06)	118±3 (96±3)	−2.74
H195A (5.46)	*low expression*											
N255A (6.52)	0.2366 [5] (9.63±0.16)	134±3 (100)	−1.59	0.0152 [5] (10.82±0.19)	118±2 (94±1)	−0.44	0.0396 [5] (10.40±0.18)	116±4 (85±3)	−0.99	1.8707 [5] (8.73±0.06)	111+5 (88±4)	−2.30

Extended Data Table 7 | Functional data (Gi/o GloSensor) for mutants of the lateral channel.

Data were acquired with MT_1 wild-type (WT) and mutants by using GloSensor to measure Gi/o-mediated cAMP inhibition via isoproterenol stimulation. Data represent means of EC_{50} (number of independent experiments in square brackets), represented as mean(pEC_{50}) ± s.e.m. as well as E_{MAX} shown as mean(%E_{MAX}) ± s.e.m. %E_{MAX} is relative to wild-type receptor in columns, and (%E_{MAX}*) is relative to melatonin activity in rows. Mutant effects were calculated by the change in relative activity, or log(E_{MAX} /EC_{50}) subtracting wild-type from mutant. ND, not determined. Dose-response curves are shown in Supplementary Figure 6.

	melatonin			ramelteon			bitopic ligand CTL 01-05-B-A05		
	EC_{50}, nM [n] (pEC_{50})	**%E_{MAX} (%E_{MAX}*)**	**Δlog (E_{MAX} / EC_{50})**	**EC50, nM [n] (pEC_{50})**	**%E_{MAX} (%E_{MAX}*)**	**Δlog (E_{MAX} / EC_{50})**	**EC_{50}, nM [n] (pEC_{50})**	**%E_{MAX} (%E_{MAX}*)**	**Δlog (E_{MAX} / EC_{50})**
WT	0.0045 [23] (11.34±0.07)	100 (100)	0	0.0035 [12] (11.45±0.15)	100 (98±2)	0	0.69 [4] (9.16±0.09)	100 (124±3)	0
A158M (4.56)	*no activity*						ND		
A190F (5.41)	0.0141 [9] (10.85±0.20)	110±4 (100)	−0.45	0.0084 [6] (11.07±0.43)	119±7 (106±6)	−0.31	5.75 [4] (8.24±0.13)	107±3 (120±3)	−0.89

Supplementary Material

Refer to Web version on PubMed Central for supplementary material.

Acknowledgements

We thank M. Chu, C. Hanson, K. Villers, J. Velasquez, and H. Shaye for technical support, and D.R. Mende for useful discussion of sequence analysis. This research was supported by the National Institutes of Health (NIH) grant R35 GM127086 (V.C.), R21 DA042298 (W.L.), R01 GM124152 (W.L.), U24DK116195 (B.L.R.), the NIMH Psychoactive Drug Screening Program contract (B.L.R.), F31-NS093917 (R.H.J.O.), the National Science Foundation (NSF) BioXFEL Science and Technology Center 1231306 (W.L., U.W., T.D.G., V.C.), EMBO ALTF 677–2014 (B.S.), HFSP long-term fellowship LT000046/2014-L (L.C.J.), postdoctoral fellowship from the Swedish Research Council (L.C.J.). C.G. kindly thanks SLAC National Accelerator Laboratory and the Department of Energy for financial support through the Panofsky fellowship. T.A.W. and W.B. acknowledge financial support from the Helmholtz Association via Programme-Oriented Funding. Parts of this research were carried out at the LCLS, a National User Facility operated by Stanford University on behalf of the U.S. Department of Energy and is supported by the U.S. Department of Energy Office of Science, Office of Basic Energy Sciences under Contract No. DE-AC02–76SF00515.

References

1. Pevet P Melatonin receptors as therapeutic targets in the suprachiasmatic nucleus. Expert Opin Ther Tar 20, 1209–1218 (2016).
2. Hardeland R, Pandi-Perumal SR & Cardinali DP Melatonin. Int J Biochem Cell Biol 38, 313–316 (2006). [PubMed: 16219483]
3. Dubocovich ML & Markowska M Functional MT1 and MT2 melatonin receptors in mammals. Endocrine 27, 101–110 (2005). [PubMed: 16217123]

4. Ganguly S, Coon SL & Klein DC Control of melatonin synthesis in the mammalian pineal gland: the critical role of serotonin acetylation. Cell Tissue Res 309, 127–137 (2002). [PubMed: 12111543]
5. Tosini G, Owino S, Guillaume JL & Jockers R Understanding melatonin receptor pharmacology: latest insights from mouse models, and their relevance to human disease. Bioessays 36, 778–787 (2014). [PubMed: 24903552]
6. Dubocovich ML et al. International Union of Basic and Clinical Pharmacology. LXXV. Nomenclature, classification, and pharmacology of G protein-coupled melatonin receptors. Pharmacol Rev 62, 343–380 (2010). [PubMed: 20605968]
7. Stoller MK Economic effects of insomnia. Clin Ther 16, 873–897; discussion 854 (1994). [PubMed: 7859246]
8. Jockers R et al. Update on melatonin receptors: IUPHAR Review 20. Brit J Pharmacol 173, 2702–2725 (2016). [PubMed: 27314810]
9. Zlotos DP Recent progress in the development of agonists and antagonists for melatonin receptors. Curr Med Chem 19, 3532–3549 (2012). [PubMed: 22680635]
10. Clarke TC, Black LI, Stussman BJ, Barnes PM & Nahin RL Trends in the use of complementary health approaches among adults: United States, 2002–2012. Natl Health Stat Report, 1–16 (2015).
11. Owen RT Ramelteon: profile of a new sleep-promoting medication. Drugs Today 42, 255–263 (2006). [PubMed: 16703122]
12. Millan MJ et al. The novel melatonin agonist agomelatine (S20098) is an antagonist at 5-hydroxytryptamine 2C receptors, blockade of which enhances the activity of frontocortical dopaminergic and adrenergic pathways. J Pharmacol Exp Ther 306, 954–964 (2003). [PubMed: 12750432]
13. Guardiola-Lemaitre B et al. Agomelatine: mechanism of action and pharmacological profile in relation to antidepressant properties. Brit J Pharmacol 171, 3604–3619 (2014). [PubMed: 24724693]
14. Johansson LC et al. XFEL structures of the human MT2 melatonin receptor reveal basis of subtype selectivity. (2019).
15. Yin J, Mobarec JC, Kolb P & Rosenbaum DM Crystal structure of the human OX2 orexin receptor bound to the insomnia drug suvorexant. Nature 519, 247–250 (2015). [PubMed: 25533960]
16. Ballesteros JA & Weinstein H in Methods in Neurosciences Vol. Volume 25 (ed Stuart C. Sealfon) 366–428 (Academic Press, 1995).
17. Katritch V et al. Allosteric sodium in class A GPCR signaling. Trends Biochem Sci 39, 233–244 (2014). [PubMed: 24767681]
18. White KL et al. Structural Connection between Activation Microswitch and Allosteric Sodium Site in GPCR Signaling. Structure 26, 259–269 (2018). [PubMed: 29395784]
19. Rasmussen SG et al. Crystal structure of the beta2 adrenergic receptor-Gs protein complex. Nature 477, 549–555 (2011). [PubMed: 21772288]
20. Cherezov V et al. High-resolution crystal structure of an engineered human beta2-adrenergic G protein-coupled receptor. Science 318, 1258–1265 (2007). [PubMed: 17962520]
21. Stauch B & Cherezov V Serial Femtosecond Crystallography of G Protein-Coupled Receptors. Ann Rev Biophys 47, 377–397 (2018). [PubMed: 29543504]
22. Isberg V et al. GPCRdb: an information system for G protein-coupled receptors. Nucleic Acids Res 44, D356–D364 (2016). [PubMed: 26582914]
23. Bento AP et al. The ChEMBL bioactivity database: an update. Nucleic Acids Res 42, D1083–1090 (2014). [PubMed: 24214965]
24. Dubocovich ML Luzindole (N-0774): a novel melatonin receptor antagonist. J Pharmacol Exp Ther 246, 902–910 (1988). [PubMed: 2843633]
25. Reppert SM, Weaver DR, Ebisawa T, Mahle CD & Kolakowski LF Cloning of a melatonin-related receptor from human pituitary. FEBS Letters 386, 219–224 (1996). [PubMed: 8647286]
26. Clement N et al. Importance of the second extracellular loop for melatonin MT1 receptor function and absence of melatonin binding in GPR50. Br J Pharmacol 175, 3281–3297 (2017). [PubMed: 28898928]

27. Azmitia EC Serotonin and brain: evolution, neuroplasticity, and homeostasis. Int Rev Neurobiol 77, 31–56 (2007). [PubMed: 17178471]
28. Tan DX et al. Melatonin: a hormone, a tissue factor, an autocoid, a paracoid, and an antioxidant vitamin. J Pineal Res 34, 75–78 (2003). [PubMed: 12485375]
29. Yu H, Dickson EJ, Jung SR, Koh DS & Hille B High membrane permeability for melatonin. J Gen Physiol 147, 63–76 (2016). [PubMed: 26712850]
30. de la Fuente Revenga M et al. Novel N-Acetyl Bioisosteres of Melatonin: Melatonergic Receptor Pharmacology, Physicochemical Studies, and Phenotypic Assessment of Their Neurogenic Potential. J Med Chem 58, 4998–5014 (2015). [PubMed: 26023814]
31. Peng Y et al. 5-HT2C Receptor Structures Reveal the Structural Basis of GPCR Polypharmacology. Cell 172, 719–730.e714 (2018). [PubMed: 29398112]
32. Pasqualetti M et al. Distribution and cellular localization of the serotonin type 2C receptor messenger RNA in human brain. Neuroscience 92, 601–611 (1999). [PubMed: 10408609]
33. The UniProt Consortium. UniProt: the universal protein knowledgebase. Nucleic Acids Res 45, D158–D169 (2017). [PubMed: 27899622]
34. Altschul SF, Gish W, Miller W, Myers EW & Lipman DJ Basic local alignment search tool. J Mol Biol 215, 403–410 (1990). [PubMed: 2231712]
35. Johnson M et al. NCBI BLAST: a better web interface. Nucleic Acids Res 36, W5–W9 (2008). [PubMed: 18440982]
36. Papadopoulos JS & Agarwala R COBALT: constraint-based alignment tool for multiple protein sequences. Bioinformatics 23, 1073–1079 (2007). [PubMed: 17332019]
37. Isberg V et al. Generic GPCR residue numbers - aligning topology maps while minding the gaps. Trends Pharmacol Sci 36, 22–31 (2015). [PubMed: 25541108]
38. Kullback S & Leibler RA On Information and Sufficiency. Ann Math Stat 22, 79–86 (1951).
39. White JF et al. Structure of the agonist-bound neurotensin receptor. Nature 490, 508–513 (2012). [PubMed: 23051748]
40. Shibata Y et al. Thermostabilization of the neurotensin receptor NTS1. J Mol Biol 390, 262–277 (2009). [PubMed: 19422831]
41. Roth CB, Hanson MA & Stevens RC Stabilization of the human beta2-adrenergic receptor TM4-TM3-TM5 helix interface by mutagenesis of Glu122(3.41), a critical residue in GPCR structure. J Mol Biol 376, 1305–1319 (2008). [PubMed: 18222471]
42. Bhattacharya S, Hall SE & Vaidehi N Agonist-induced conformational changes in bovine rhodopsin: insight into activation of G-protein-coupled receptors. J Mol Biol 382, 539–555 (2008). [PubMed: 18638482]
43. Klco JM, Nikiforovich GV & Baranski TJ Genetic analysis of the first and third extracellular loops of the C5a receptor reveals an essential WXFG motif in the first loop. J Biol Chem 281, 12010–12019 (2006). [PubMed: 16505476]
44. Caffrey M & Cherezov V Crystallizing membrane proteins using lipidic mesophases. Nat Protoc 4, 706–731 (2009). [PubMed: 19390528]
45. Liu W, Ishchenko A & Cherezov V Preparation of microcrystals in lipidic cubic phase for serial femtosecond crystallography. Nat Protoc 9, 2123–2134 (2014). [PubMed: 25122522]
46. Weierstall U et al. Lipidic cubic phase injector facilitates membrane protein serial femtosecond crystallography. Nat Commun 5, 3309 (2014). [PubMed: 24525480]
47. Boutet S & Williams GJ The Coherent X-ray Imaging (CXI) instrument at the Linac Coherent Light Source (LCLS). New J Phys 12, 035024 (2010).
48. Hart P et al. The Cornell-SLAC Pixel Array Detector at LCLS. SLAC-PUB-15284, doi:10.1109/NSSMIC.2012.6551166 (2012).
49. Barty A et al. Cheetah: software for high-throughput reduction and analysis of serial femtosecond X-ray diffraction data. J Appl Crystallogr 47, 1118–1131 (2014). [PubMed: 24904246]
50. White TA et al. CrystFEL: a software suite for snapshot serial crystallography. J Appl Crystallogr 45, 335–341 (2012).
51. Leslie AG The integration of macromolecular diffraction data. Acta Crystallogr D 62, 48–57 (2006). [PubMed: 16369093]

52. Duisenberg A Indexing in single-crystal diffractometry with an obstinate list of reflections. J Appl Crystallogr 25, 92–96 (1992).
53. Kabsch W XDS. Acta Crystallogr D 66, 125–132 (2010). [PubMed: 20124692]
54. White TA et al. Recent developments in CrystFEL. J Appl Crystallogr 49, 680–689 (2016). [PubMed: 27047311]
55. McCoy AJ et al. Phaser crystallographic software. J Appl Crystalogr 40, 658–674 (2007).
56. Murshudov GN et al. REFMAC5 for the refinement of macromolecular crystal structures. Acta Crystallogr D 67, 355–367 (2011). [PubMed: 21460454]
57. BUSTER v. 2.10.2 (Global Phasing Ltd., Cambridge, United Kindom, 2017).
58. Emsley P, Lohkamp B, Scott WG & Cowtan K Features and development of Coot. Acta Crystallogr D 66, 486–501 (2010). [PubMed: 20383002]
59. Schuttelkopf AW & van Aalten DM PRODRG: a tool for high-throughput crystallography of protein-ligand complexes. Acta Crystallogr D 60, 1355–1363 (2004). [PubMed: 15272157]
60. Chen VB et al. MolProbity: all-atom structure validation for macromolecular crystallography. Acta Crystallogr D 66, 12–21 (2010). [PubMed: 20057044]
61. Adams PD et al. PHENIX: a comprehensive Python-based system for macromolecular structure solution. Acta Crystallogr D Biol Crystallogr 66, 213–221 (2010). [PubMed: 20124702]
62. Alexandrov AI, Mileni M, Chien EY, Hanson MA & Stevens RC Microscale fluorescent thermal stability assay for membrane proteins. Structure 16, 351–359 (2008). [PubMed: 18334210]
63. Depreux P et al. Synthesis and structure-activity relationships of novel naphthalenic and bioisosteric related amidic derivatives as melatonin receptor ligands. J Med Chem 37, 3231–3239 (1994). [PubMed: 7932550]
64. Yous S et al. Novel naphthalenic ligands with high affinity for the melatonin receptor. J Med Chem 35, 1484–1486 (1992). [PubMed: 1315395]
65. Lomize MA, Pogozheva ID, Joo H, Mosberg HI & Lomize AL OPM database and PPM web server: resources for positioning of proteins in membranes. Nucleic Acids Res 40, D370–376 (2012). [PubMed: 21890895]
66. Berman HM et al. The Protein Data Bank. Nucleic Acids Res 28, 235–242 (2000). [PubMed: 10592235]
67. Kabsch W & Sander C Dictionary of protein secondary structure: pattern recognition of hydrogen-bonded and geometrical features. Biopolymers 22, 2577–2637 (1983). [PubMed: 6667333]
68. Cock PJ et al. Biopython: freely available Python tools for computational molecular biology and bioinformatics. Bioinformatics 25, 1422–1423 (2009). [PubMed: 19304878]
69. Henikoff S & Henikoff JG Performance evaluation of amino acid substitution matrices. Proteins 17, 49–61 (1993). [PubMed: 8234244]
70. Krogh A, Larsson B, von Heijne G & Sonnhammer EL Predicting transmembrane protein topology with a hidden Markov model: application to complete genomes. J Mol Biol 305, 567–580 (2001). [PubMed: 11152613]
71. Senes A, Gerstein M & Engelman DM Statistical analysis of amino acid patterns in transmembrane helices: the GxxxG motif occurs frequently and in association with beta-branched residues at neighboring positions. J Mol Biol 296, 921–936 (2000). [PubMed: 10677292]
72. O'Boyle NM et al. Open Babel: An open chemical toolbox. J Cheminformatics 3, 33 (2011).
73. Kozlikova B et al. CAVER Analyst 1.0: graphic tool for interactive visualization and analysis of tunnels and channels in protein structures. Bioinformatics 30, 2684–2685 (2014). [PubMed: 24876375]
74. Schrödinger LLC The PyMOL Molecular Graphics System, Version 1.8 (2015).
75. Abagyan R, Totrov M & Kuznetsov D ICM—A new method for protein modeling and design: Applications to docking and structure prediction from the distorted native conformation. J Comput Chem 15, 488–506 (1994).
76. Halgren TA Merck molecular force field. I. Basis, form, scope, parameterization, and performance of MMFF94. J Comput Chem 17, 490–519 (1996).
77. Zhang H et al. Structural basis for selectivity and diversity in angiotensin II receptors. Nature 544, 327–332 (2017). [PubMed: 28379944]

78. Jo S, Kim T, Iyer VG & Im W CHARMM-GUI: a web-based graphical user interface for CHARMM. J Comput Chem 29, 1859–1865 (2008). [PubMed: 18351591]

79. Liu W et al. Serial femtosecond crystallography of G protein-coupled receptors. Science 342, 1521–1524 (2013). [PubMed: 24357322]

80. Vanommeslaeghe K et al. CHARMM general force field: A force field for drug-like molecules compatible with the CHARMM all-atom additive biological force fields. J Comput Chem 31, 671–690 (2010). [PubMed: 19575467]

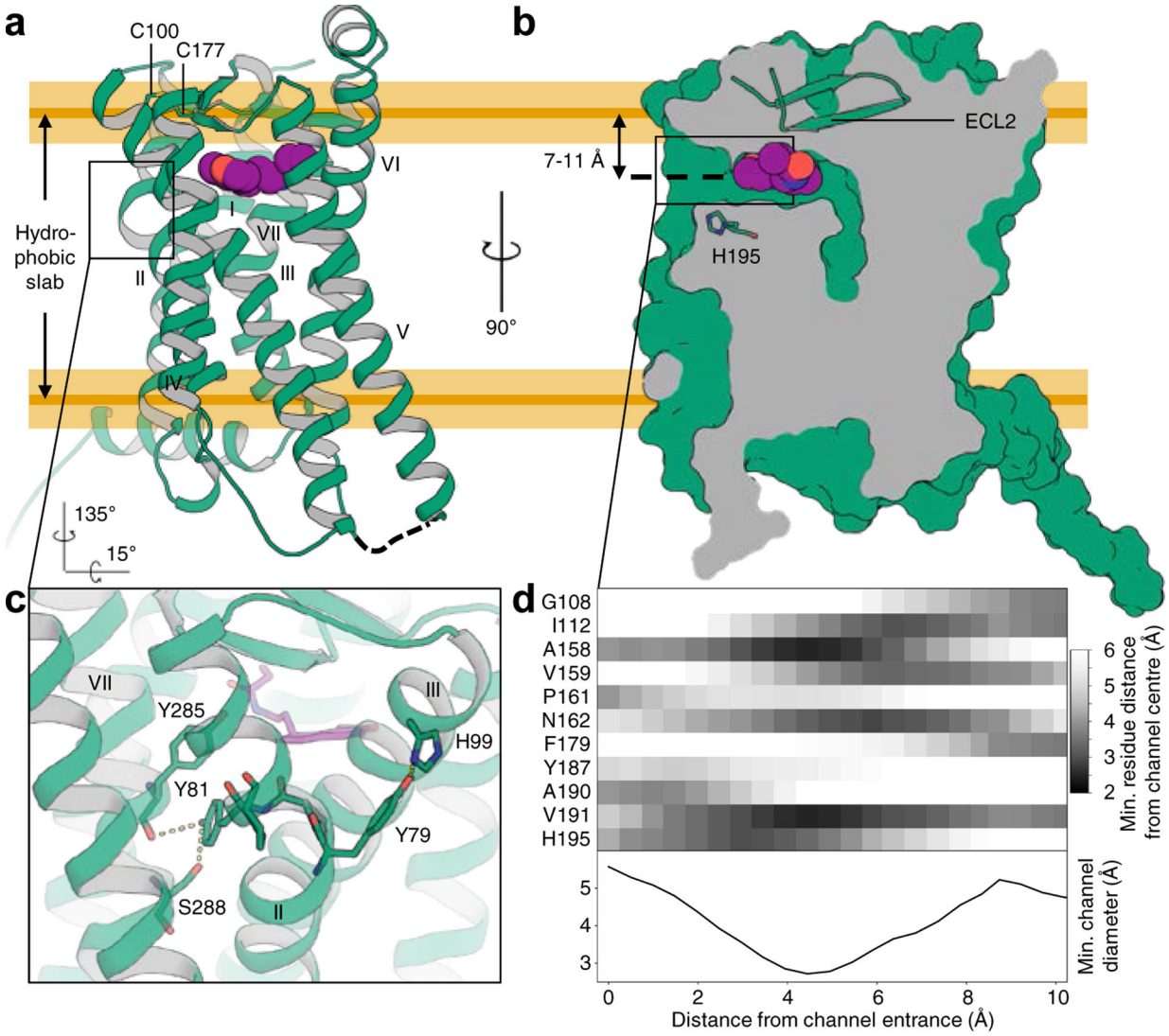

Fig. 1 |. Structural features of MT_1.

a, Overall architecture of MT_1 (green; disulfide yellow, helices labeled with Roman numerals) bound to ramelteon (purple). ICL3 was replaced by a fusion protein and is shown as a dashed line. Approximate boundaries of the hydrophobic slab corresponding to the lipid tails are derived from MD simulation and indicated by orange lines (yellow shaded areas represent s.d.). ECL2 closes off the binding site to the extracellular space. **b**, Section through the receptor illustrating the lateral ligand access channel. **c**, Details of the unique YPYP motif in helix II that forms a bulge in proximity to the ligand. Residues are shown as green sticks, and hydrogen bonds as dashed lines. **d**, Proximity matrix of pore-lining residues, and minimum diameter profile across the length of the channel, calculated using spherical probes.

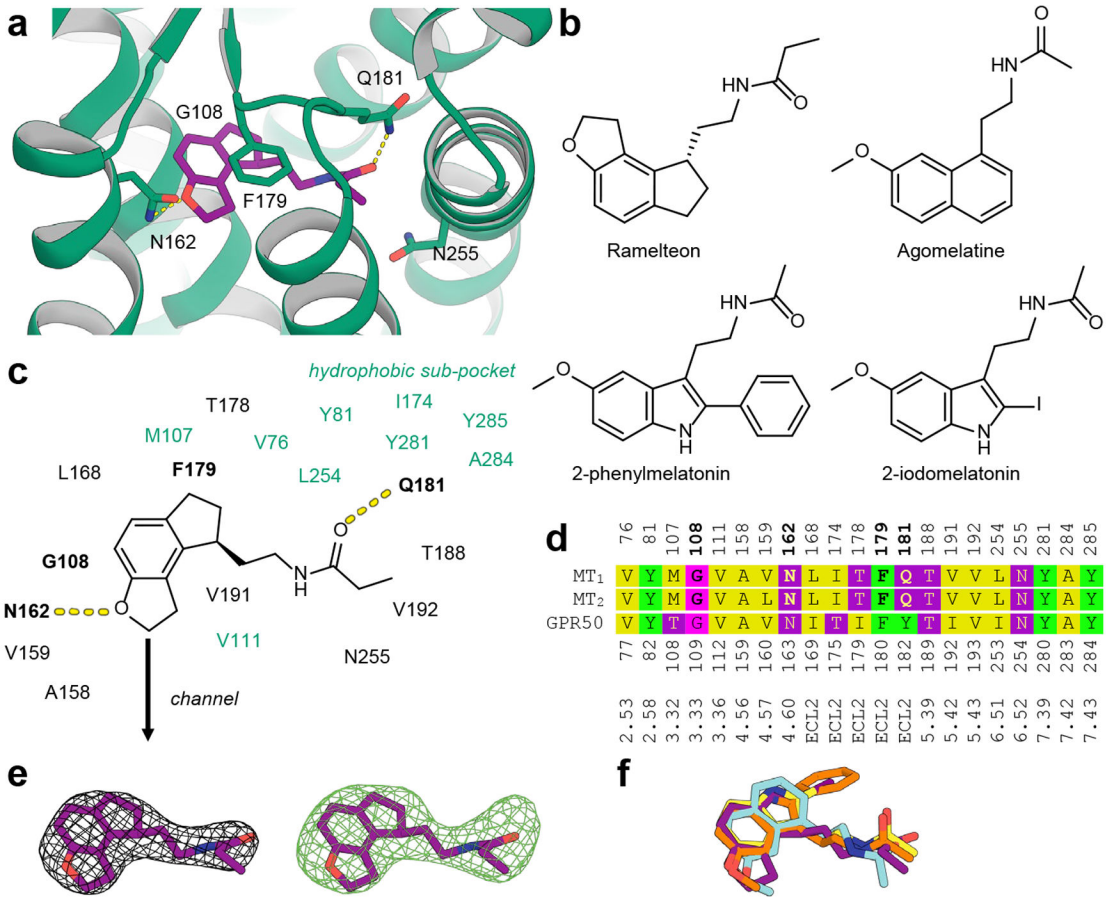

Fig. 2 |. Ligand recognition at MT_1.

a, Ramelteon (purple) forms specific interactions with side chains of N162 and Q181 of MT_1 (green), and stacks with F179 (all side chains shown as green sticks). **b**, Chemical structures of melatonergic ligands that were co-crystallised with MT_1 in this work. **c**, Binding site composition and interactions of ramelteon as a representative for all four complexes. The hydrophobic sub-pocket accommodating substituents at the 2 position of indole-like ligands is shown in green. **d**, Structure-guided sequence alignment of MT_1 (residue numbering above), MT_2, and GPR50 (residue numbering below) binding site residues. Ligand-interacting residues in MT_1 and MT_2 are highlighted in bold, and Ballesteros-Weinstein residue numbering is provided for reference. **e**, $2mF_o-DF_c$ electron density map (grey mesh) in the binding site of the MT_1-ramelteon complex, contoured at 1.0 **σ**, and simulated annealing mF_o-DF_c omit map (green mesh), contoured at 3.0 **σ**. Electron density maps for other ligands are shown in Extended Data Fig. 1. **f**, Overlay of experimental ligand conformations of ramelteon (purple), 2-pmt (orange), 2-iodomelatonin (yellow), and agomelatine (cyan) after receptor superimposition. The conformations of receptor side chains in the binding site are very similar between the complexes and are omitted for clarity.

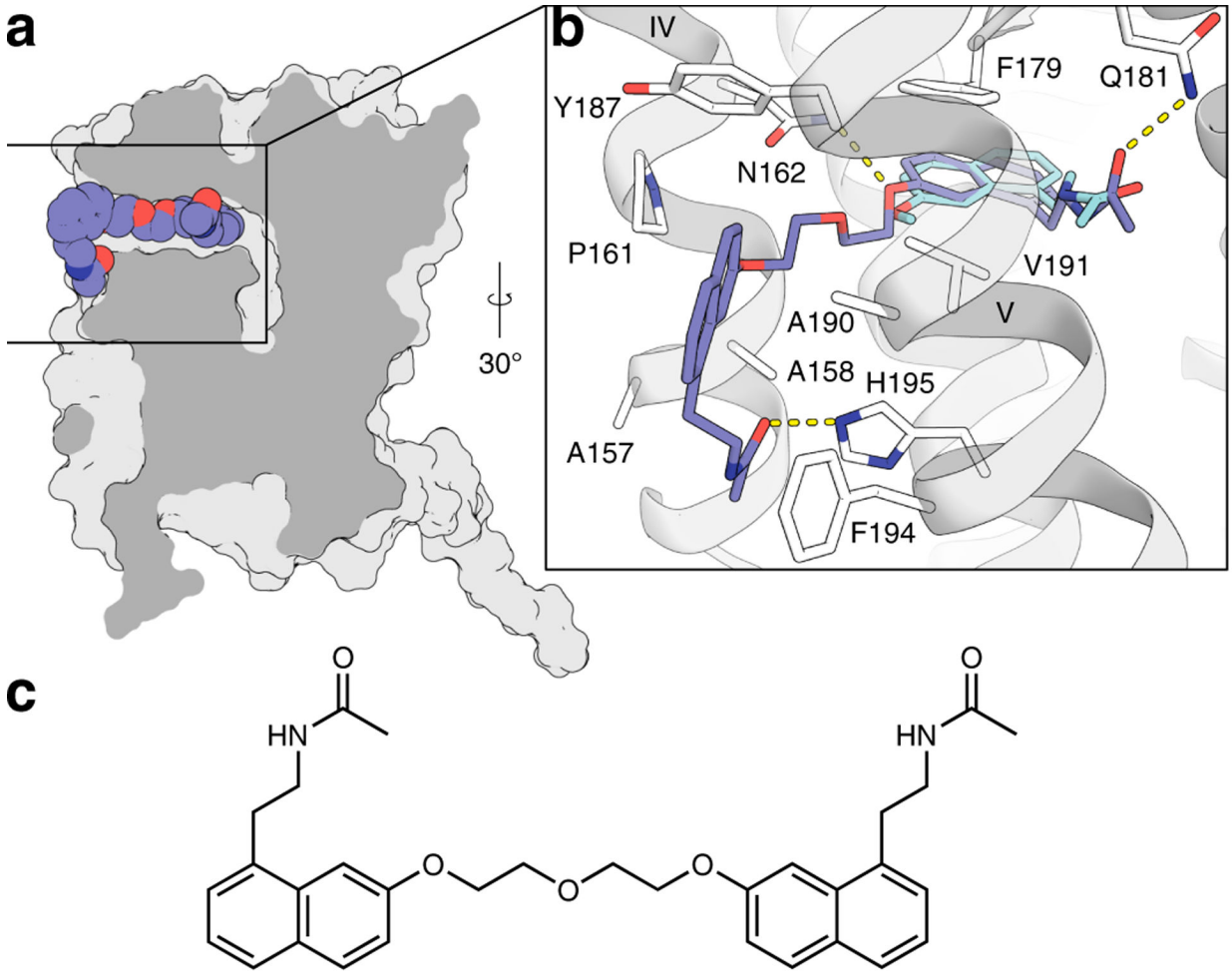

Fig. 3 |. Docking model of bitopic ligand.

a, Section through MT_1 (grey) showing the best docked pose of the bitopic ligand CTL 01–05-B-A05 (spheres with slate blue carbons). **b**, Details of receptor ligand interactions. Dashed lines represent hydrogen bonds between ligand moieties and receptor residues $N162^{4.60}$, $Q181^{ECL2}$, and $H195^{5.46}$, respectively. **c**, Chemical structure of CTL 01–05-B-A05. The ligand protrudes from the lateral channel between helices IV and V. Its core shows minor displacement compared to the experimentally determined conformation of agomelatine (cyan sticks), and it forms favourable interactions with several residues (white sticks) in the periphery of the channel.

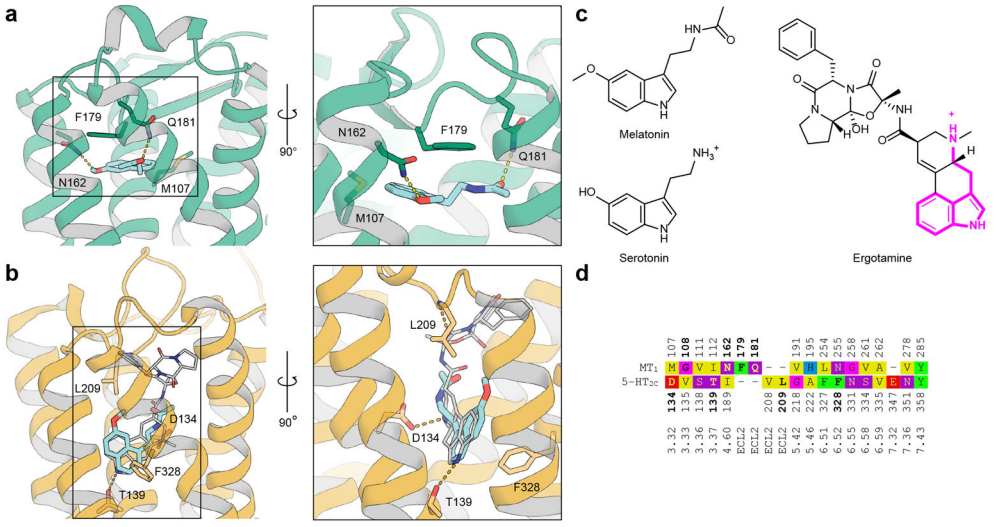

Fig. 4 |. Comparison between MT_1 and 5-HT_{2C}.

a, Crystal structure of agomelatine (cyan sticks, $pK_i(MT_1)$=8.8) bound to MT_1 (green cartoon). Important residues in the binding site are shown as sticks with green carbons. **b**, Crystal structure of ergotamine (grey sticks) bound to 5-HT_{2C} (orange cartoon), and docking model of agomelatine (cyan sticks, pK_i(5-HT_{2C})[13]=6.2). **c**, Chemical structures of melatonin, serotonin, and ergotamine with the substructure shared between serotonin and ergotamine highlighted (magenta). **d**, Structure-guided sequence alignment in the binding sites of MT_1 and 5-HT_{2C} receptors with reference sequence numbering (above / below), and Ballesteros-Weinstein numbering (bottom). Residues participating in tight ligand interactions in the respective structure are bold.